DOE/ET-53088-76 IFSR #76

3D NONLINEAR INCOMPRESSIBLE MHD CALCULATIONS

A. Y. Aydemir and D. C. Barnes

Institute for Fusion Studies
University of Texas at Austin
Austin, Texas 78712

January 1983

3D Nonlinear Incompressible MHD Calculations

A. Y. Aydemir and D. C. Barnes

Institute for Fusion Studies

The University of Texas, Austin, Texas 78712

ABSTRACT

An algorithm is developed for 3D nonlinear, resistive, incompressible magnetohydrodynamic calculations in a cylindrical geometry. The non-reduced primitive MHD equations are used. The state variables are expanded in Fourier series in the poloidal and axial coordinates, while a finite difference scheme is used in the radial direction. Applications to m=1 tearing mode calculations in tokamaks, and the self reversal of a reversed field pinch are presented.

1. INTRODUCTION

In magnetic fusion research, magnetohydrodynamic (MHD) equations have been used quite successfully in studying gross dynamics, and macroscopic equilibrium and stability problems of fusion plasmas. Following the evolution of plasmas from an initial non-equilibrium to an equilibrium state necessitates the solution of nonlinear MHD equations as an initial-boundary value problem. Similarly, modification of a given equilibrium by possible ideal or resistive instabilities can only be followed in time using a nonlinear initial value algorithm. Several multidimensional codes of various forms have been in use for quite some time now. Excellent reviews can be found in Brackbill[1] and Schnack[2].

In recent years, the emphasis in large scale MHD computations has shifted to the use of Fourier transform techniques,since in general such codes tend to be more efficient and accurate,especially when only a relatively small number of modes are needed. Orszag has been a proponent of the use of spectral methods in fluid dynamics calculations for many years[3]. In magnetic fusion research where instabilities tend to nonlinearly develop singularities or large gradients in radial direction, using Fourier expansions in poloidal and toroidal coordinates and finite-difference methods in the radial direction has proved to be a more efficient method. Park. et. al., used this technique and the reduced MHD equations in the high-β ordering[4] to study the second stability regime of ballooning modes [5,6]. A series of codes using similar methods and the reduced MHD equations has been developed at Oak Ridge National Laboratory

and used to study the interaction of tearing modes in cylindrical and toroidal geometries [7-9].

Reduced MHD equations are based on expansions in the inverse aspect ratio, ratio of the minor to major radius of a torus, and make use of certain ordering assumptions about the relative strength of various physical quantities. In particular, in the low-β ordering [10],

$$B_\theta/B_\zeta \sim O(\varepsilon), \text{and} \qquad (1)$$
$$p/B_\zeta^2 \sim O(\varepsilon^2),$$

while the high-β ordering assumes $p/B_\zeta^2 \sim O(\varepsilon)$. B_θ, B_ζ are the poloidal and toroidal field strengths, respectively. p is the plasma presure and ε, the small parameter used in the expansions, is the inverse aspect ratio. For many fusion devices other than tokamaks, these assumptions are not valid, and one is forced to abandon the reduced MHD equations.

In this paper, we describe a new algorithm for solving the primitive, nonlinear, resistive MHD equations in three dimensions using a Fourier expansion method. In contrast to methods based on reduced MHD equations, the poloidal field is not assumed small relative to the toroidal field. However, the plasma motion is assumed incompressible; thus, the compressional modes are eliminated, and only the shear Alfven time scale remains. The resulting algorithm is very efficient, since MHD instability phenomena occur on this slower time scale.

Besides the incompressibility of the flow field, no other assumptions are made, and the full set of nonlinear MHD equations are solved as an initial-boundary value problem in a cylindrical geometry. With periodic boundary conditions in the toroidal direction, the computational domain is topologically equivalent to a torus. All effects of toroidal curvature, however, are missing in our calculations, and a proper treatment of toroidal corrections is left for a future work.

In Section 2, we review the standard set of incompressible MHD equations. Numerical methods, a mixture of Fourier transform and finite-difference techniques, are discussed in Section 3. Results from linear and nonlinear evolution of m=1 mode in small and large aspect ratio tokamaks, and the self reversal of an RFP are given in Section 4. Section 5 summarizes the results described here.

2. THE EQUATIONS

The incompressible,resistive MHD equations are written in the following form:

$$\frac{\partial \underset{\sim}{u}}{\partial t} = -\nabla\cdot\underset{\sim}{uu} + \underset{\sim}{J}\times\underset{\sim}{B} - \nabla p, \tag{2}$$

$$\frac{\partial \underset{\sim}{B}}{\partial t} = -\nabla\times\underset{\sim}{E}, \tag{3}$$

$$\underset{\sim}{E} = -\underset{\sim}{u}\times\underset{\sim}{B} + \frac{1}{S}\underset{\sim}{J}, \tag{4}$$

$$\underset{\sim}{J} = \nabla\times\underset{\sim}{B}, \tag{5}$$

$$\nabla\cdot\underset{\sim}{u} = 0, \tag{6}$$

$$\nabla\cdot\underset{\sim}{B} = 0. \tag{7}$$

where $\underset{\sim}{u}$,$\underset{\sim}{B}$, and $\underset{\sim}{E}$ are velocity,magnetic and electric fields,respectively. $\underset{\sim}{J}$ is the current density, and p is the scalar pressure field. There is no equation for time-advancing p;its instantaneous value is determined by the incompressibilty condition $\nabla\cdot\underset{\sim}{u}=0$, which serves as the equation of state.

Variables have been normalized as follows:

$\underset{\sim}{r} \rightarrow \underset{\sim}{r}/a$ $\qquad$ $\underset{\sim}{B} \rightarrow \underset{\sim}{B}/B_{\theta_o}$

$t \rightarrow t/\tau_{hp}$ $\qquad$ $\underset{\sim}{u} \rightarrow \underset{\sim}{u}/u_{hp}$

$\rho \rightarrow \rho/\rho_o=1$ $\qquad$ $p \rightarrow p/u_a^2$

where a is the minor radius, and B_{θ_o} is a characteristic poloidal field strength. The mass density ρ is assumed to be constant (unity), which is consistent with Eq.(6) and a uniform initial state. S is the ratio of the diffusion time $\tau_r = \mu_o a^2/\eta_o$ to the poloidal Alfven time $\tau_{hp} = a/u_{hp}$, where $u_{hp} = B_{\theta_o}/(\mu_o \rho_o)^{1/2}$, and η_o is a characteristic value for resistivity.

Resistivity is not calculated self-consistently. In general it is an ad hoc function of space and time. In some tokamak applications, it is assumed to have the functional form

$$\eta(r) = E_{\zeta_{wall}}/J_\zeta(r;t=0),$$

which prevents decay of the axial current in the absence of unstable modes [11].

3. NUMERICAL METHODS

Eqs.(2-7) are solved by a combination of Fourier expansions in the azimuthal and toroidal directions, and finite difference techniques in the radial direction. The truncated Fourier expansions provide an exact representation of the azimuthal and toroidal derivatives. As the numerical results of Section 4 demonstrate, the resulting method is highly accurate in resolving fine radial structures that develop during linear and nonlinear calculations when a fine radial grid is employed.

The incompressible equation of state, Eq. 6, results in an implicit equation for the pressure field p. In addition, a restrictive condition on the time step associated with the resistive diffusion and the small radial grid spacing is avoided by implicitly differencing the diffusion terms in Eqs.(3,4). These implicit equations are easily inverted because of the decoupling afforded by Fourier expansions.

We turn next to the description of coordinates and the Fourier expansions of the state variables.

3.1 Coordinates and Fourier Expansions

The coordinates for our cylindrical problem are (r,θ,ζ), where r is the radius, θ is the azimuthal angle, and the angle ζ is related to the usual cylindrical z by $z=R_o\zeta$. R_o is the major radius of the torus.

All variables are expanded in double Fourier series in the periodic directions θ, and ζ. If the initial equlibrium is characterized by the fields

$$B_{\theta_o} = \sum_{m,n} a_{mn}\cos(m\theta+n\zeta),$$

$$B_{\zeta_o} = \sum_{m,n} b_{mn}\cos(m\theta+n\zeta),$$

where usually only the m=0,n=0 coefficients are non-zero,and if the parity of the perturbation is chosen accordingly, Eqs.(2-7) generate only pure sine

or cosine series. Sine series are required for B_r, u_θ, and u_ζ, whereas, u_r, B_θ, B_ζ, and p are expanded in cosine series:

$$\underset{\sim}{U}_s(r,\theta,\zeta) = \sum_{m,n} i\underset{\sim}{U}_s(r;mn)e^{i(m\theta+n\zeta)}$$

$$\underset{\sim}{U}_c(r,\theta,\zeta) = \sum_{m,n} \underset{\sim}{U}_c(r;mn)e^{i(m\theta+n\zeta)} \qquad (8)$$

where

$$\underset{\sim}{U}_s(r,\theta,\zeta) = \left[B_r(r,\theta,\zeta), u_\theta(r,\theta,\zeta), u_\zeta(r,\theta,\zeta)\right]^t,$$

$$\underset{\sim}{U}_c(r,\theta,\zeta) = \left[u_r(r,\theta,\zeta), B_\theta(r,\theta,\zeta), B_\zeta(r,\theta,\zeta), p(r,\theta,\zeta)\right]^t,$$

and

$$\underset{\sim}{U}_s(r;-m,-n) = -\underset{\sim}{U}_s(r;m,n), \qquad \underset{\sim}{U}_c(r;-m,-n) = \underset{\sim}{U}_c(r;m,n).$$

Because of odd/even parity of the coefficients, only half of them are calculated and stored.

The convolution sums resulting from the $\underset{\sim}{u}\underset{\sim}{u}$ and $\underset{\sim}{J}\times\underset{\sim}{B}$ terms in Eq.(2), and the $\underset{\sim}{u}\times\underset{\sim}{B}$ term in Eq.(4) are evaluated directly, without using Fast Fourier Transform techniques [3]. However, on vector machines such as Cray-1, the summations can be vectorized over the radial mesh points, which results in an efficient code.

A result of the Fourier decomposition is the almost trivial linearization of the equations. The code can be run either in a linear mode, where only one Fourier coefficient is calculated, or in a nonlinear mode where all coefficients are advanced in time simultaneously.

We turn next to the temporal differencing of the equations resulting from these Fourier expansions.

3.2 Temporal Differencing

The variables are advanced in time by a first order predictor-corrector scheme. Diffusion terms are treated implicitly in order to avoid stringent Courant conditions based on the radial mesh size :

$$\underset{\sim}{u}^{*} = \underset{\sim}{u}^{n} + \delta t(-\nabla\cdot\underset{\sim}{u}^{n}\underset{\sim}{u}^{n} + \underset{\sim}{J}^{n}\times\underset{\sim}{B}^{n} - \nabla p^{*}) \tag{9}$$

$$\underset{\sim}{B}^{*} = \underset{\sim}{B}^{n} + \delta t(\nabla\times\underset{\sim}{u}^{n}\times\underset{\sim}{B}^{n} - \nabla\times\frac{1}{S}\nabla\times\underset{\sim}{B}^{*}) \tag{10}$$

$$\underset{\sim}{u}^{n+1} = \underset{\sim}{u}^{n} + \delta t(-\nabla\cdot\underset{\sim}{u}^{*}\underset{\sim}{u}^{*} + \underset{\sim}{J}^{*}\times\underset{\sim}{B}^{*} - \nabla p^{n+1}) \tag{11}$$

$$\underset{\sim}{B}^{n+1} = \underset{\sim}{B}^{n} + \delta t(\nabla\times\underset{\sim}{u}^{*}\times\underset{\sim}{B}^{*} - \nabla\times\frac{1}{S}\nabla\times\underset{\sim}{B}^{*}) \tag{12}$$

As stated earlier,there is no equation for time advancing the pressure field,p; Before Eq.(9) can be solved for $\underset{\sim}{u}^*$, p^* is determined by inverting the following elliptic equation

$$\nabla^2 p^* = \frac{1}{\delta t}\nabla\cdot\underset{\sim}{u}^n - \nabla:\underset{\sim}{u}^n\underset{\sim}{u}^n + \nabla\cdot(\underset{\sim}{J}^n\times\underset{\sim}{B}^n), \qquad (13)$$

which is obtained by taking the divergence of Eq.(9) and letting $\nabla\cdot\underset{\sim}{u}^*=0$. This method,first used by Harlow [12], ensures that the velocity field at the new time step is divergence-free, even if $\underset{\sim}{u}^n$ is not. Because of the Fourier expansions, (13) is a one dimensional equation for the Fourier amplitudes p(r;mn). The resulting tri-diagonal system is inverted using standard techniques [13].

The implicit part of Eq.(10) results in a block tri-diagonal system for $\underset{\sim}{B}^*$. Inversion of this system, and the simpler scalar system for the pressure are vectorized over the Fourier coefficients on Cray-1. This vectorization requires storing the relevant matrices for all the Fourier coefficients during the inversions. The resulting increase in storage requirements is more than compensated by the decrease in CPU time. The description of the algorithm is completed by specifying the radial differencing and the boundary conditions.

3.3 Radial Differencing

Beacause of the Fourier decomposition in θ and ζ directions, a finite-difference mesh is used only in the radial direction. To eliminate decoupling of odd and even mesh points, variables are staggered on this mesh as follows:

- $u_r(r;mn), B_r(r;mn), E_\theta(r;mn), E_\zeta(r;mn), J_\theta(r;mn)$, and $J_\zeta(r;mn)$ are defined at cell boundaries, $(r_i,\ i=0,1,..,I)$, and
- $u_\theta(r;mn), u_\zeta(r;mn), B_\theta(r;mn), B_\zeta(r;mn), E_r(r;mn), J_r(r;mn)$, and $p(r,mn)$ are defined at cell centers, $(r_{i+1/2}\ ,\ i=-1,0,1,..,I)$.

With this staggered mesh, the vector identity $\nabla\cdot\nabla\times\underset{\sim}{A} = 0$ is satisfied identically by the finite difference equations if the divergence and curl operators are defined as follows:

$$\nabla\cdot\underset{\sim}{u}_{i+1/2} = \frac{r_{i+1}\,u_{r_{i+1}} - r_i\,u_{r_i}}{r_{i+1/2}\,(r_{i+1} - r_i)} + \frac{im}{r_{i+1/2}}\,u_{\theta\,i+1/2} + \frac{in}{R_o}u_{\zeta\,i+1/2}, \quad (14)$$

$$\nabla\times\underset{\sim}{u}_i = \hat{r}\left\{\frac{im}{r_{i+1/2}}u_{\zeta\,i+1/2} - \frac{in}{R_o}u_{\theta\,i+1/2}\right\} +$$

$$\hat{\theta}\left\{\frac{in}{R_o}u_{r_i} - \frac{u_{\zeta\,i+1/2} - u_{\zeta\,i-1/2}}{\delta r_i}\right\} + \quad (15)$$

$$\hat{\zeta}\left\{\frac{(r_{i+1/2}\,u_{\theta\,i+1/2} - r_{i-1/2}\,u_{\theta\,i-1/2}}{r_i\,\delta r_i} - \frac{im}{r_i}u_{r_i}\right\},$$

where $\delta r_i = r_{i+1/2} - r_{i-1/2}$.

To ensure that the velocity field is exactly divergence free, the Laplacian operator in Eq.(13) has to be defined in a way consistent with Eq.(14). In the predictor step this is accomplished by substituting $\underset{\sim}{u}^*$ from Eq.(9) into Eq.(14) and letting $\nabla\cdot\underset{\sim}{u}^*_{i+1/2} = 0$. The resulting finite-difference form of Eq.(13) is a set of tridiagonal systems for each of the Fourier harmonics,

$$-a_i\, p^*_{i-1/2} + \left\{ a_i + c_i + \left[\frac{m^2}{r^2_{i+1/2}} + \frac{n^2}{R_o^2} \right] \right\} p^*_{i+1/2} - c_i p^*_{i+3/2}$$

$$= -\left\{ \frac{1}{\delta t}\nabla\cdot\underset{\sim}{u}^n_{i+1/2} + \nabla\cdot(\underset{\sim}{J}\times\underset{\sim}{B})^n_{i+1/2} - \nabla:(\underset{\sim}{uu})^n_{i+1/2} \right\}, \qquad (13')$$

where

$$a_i = \frac{r_i}{\delta r_i\, r_{i+1/2}\, (r_{i+1} - r_i)}, \text{ and } c_i = \frac{r_{i+1}}{\delta r_{i+1}\, r_{i+1/2}\, (r_{i+1} - r_i)}.$$

These equations have a solution $p^*_{i+1/2}$, which, when substituted into Eq.(9), guarantees that $\underset{\sim}{u}^*$ is solenoidal. The corrector step is treated in the same way.

The curl operator of Eq.(15) is used in differencing the equations for the $\underset{\sim}{B}$ field; thus, taking the divergence, as defined by Eq.(14), of Eqs. 10 and 12, we obtain

$$\nabla\cdot\underset{\sim}{B}^* = \nabla\cdot\underset{\sim}{B}^n, \text{ and}$$

$$\nabla\cdot\underset{\sim}{B}^{n+1} = \nabla\cdot\underset{\sim}{B}^n,$$

respectively. Therefore,the magnetic field remains solenoidal also if $\nabla \cdot \underset{\sim}{B} = 0$ initially.

3.4 Boundary Conditions

- Coordinate Axis

The requirement that the physical variables $\underset{\sim}{u}$, $\underset{\sim}{B}$, p, etc., be single-valued at the origin imposes certain regularity conditions on them.

For any scalar p with the expansion

$$p(r,\theta,\zeta) = \sum_{m,n} p(r;mn)e^{i(m\theta + n\zeta)},$$

if $p(0,\theta,\zeta)$ is to be single-valued, we need

$$\lim_{r\to 0} \frac{\partial p}{\partial \theta} = 0,$$

from which we obtain

$$p(r=0;mn) = 0 \text{ for } m \neq 0. \qquad (16)$$

For any vector $\underset{\sim}{u}$,

$$\underset{\sim}{u}(r,\theta,\zeta) = \sum_{m,n} \underset{\sim}{u}(r;mn)e^{i(m\theta + n\zeta)},$$

where $\underset{\sim}{u}(r;mn)$ may be complex,

$$\lim_{r\to 0} \frac{\partial \underset{\sim}{u}}{\partial \theta} = 0$$

leads to

$$u_\zeta(0;mn) = 0 \text{ for } m\neq 0, \tag{17}$$

and

$$imu_r(0;mn) - u_\theta(0;mn) = 0 \tag{18}$$

$$u_r(0;mn) + imu_\theta(0,mn) = 0.$$

The homogeneous system (18) has non-trivial solutions only for $|m|=1$, from which we obtain the following regularity conditions:

$$u_r(0;mn) + imu_\theta(0;mn) = 0 \text{ for } |m| = 1,$$

$$u_r(0;mn) = 0, \text{ and } u_\theta(0;mn) = 0 \text{ for } |m| \neq 1. \tag{19}$$

The conditions for the symmetric tensor $\underset{\sim}{u}\underset{\sim}{u}$ appearing in Eq.(2) are derived similarly. Letting $\overset{\leftrightarrow}{T} = \underset{\sim}{u}\underset{\sim}{u}$, and using

$$\lim_{r\to 0} \frac{\partial}{\partial \theta} \overset{\leftrightarrow}{T} = \overset{\leftrightarrow}{0},$$

we obtain the following conditions,where we have used

$$u_\alpha\, u_\beta \equiv \sum_{\substack{m'+m''=m \\ n'+n''=n}} u_\alpha(r;m'n')u_\beta(r;m''n''). \tag{20}$$

i) m=0:

$$\begin{aligned} u_r u_\theta &= 0 \\ u_r u_\zeta &= 0 \\ u_\theta u_\zeta &= 0 \\ u_r u_r - u_\theta u_\theta &= 0 \end{aligned} \tag{21}$$

$u_r u_r$, $u_\theta u_\theta$, and $u_\zeta u_\zeta$ can be finite at r=0.

ii) |m|=1

$$\begin{aligned} u_r u_r &= 0 \\ u_r u_\theta &= 0 \\ u_\theta u_\theta &= 0 \\ u_\zeta u_\zeta &= 0 \\ u_r u_\zeta + im\, u_\theta u_\zeta &= 0 \end{aligned} \tag{22}$$

$u_r u_\zeta$, and $u_\theta u_\zeta$ can be finite.

iii) |m|=2

$$\begin{aligned} u_r u_\zeta &= 0 \\ u_\theta u_\zeta &= 0 \\ u_\zeta u_\zeta &= 0 \\ 2u_r u_r + imu_r u_\theta &= 0 \\ 2u_\theta u_\theta - imu_r u_\theta &= 0 \end{aligned} \tag{23}$$

$u_r u_r$, $u_\theta u_\theta$, and $u_r u_\theta$ can be finite.

iv) For $|m| > 2$, $\overleftrightarrow{T} = \overleftrightarrow{0}$ at r=0.

Since these conditions should directly follow from those imposed on $\underset{\sim}{u}$ itself, they are merely used as a first order check on the convolution sums in Eq.(20).

On our staggered mesh, which is extended to $r < 0$ as shown in Fig. 1, the conditions in Eqs. 16,17,and 19 are implemented by odd/even reflection about r=0 of those variables defined at the cell centers.

- The outer boundary

The cylindrical wall is usually, but not necessarily, a flux surface with

$$B_r = 0$$

$$u_r = 0. \qquad (24)$$

The parallel components of $\underset{\sim}{u}$ are determined by the free-slip conditions

$$\hat{\theta}\cdot\nabla\times\underset{\sim}{u} = \hat{\zeta}\cdot\nabla\times\underset{\sim}{u} = 0 \text{ for all (m/n).}$$

Except for a possible symmetric axial field, the parallel components of $\underset{\sim}{E}$ vanish at the wall:

$$E_\theta = 0 \text{ for all } (m/n), \text{ and} \tag{25}$$

$$E_\zeta = E_{\zeta_{wall}} \text{ for } (m/n)=(0/0); E_\zeta = 0 \text{ otherwise.}$$

Consistent with Eq.(25), the $\underset{\sim}{B}$ field satisfies

$$\hat{\theta}\cdot\nabla\times\underset{\sim}{B} = 0 \text{ for all } (m/n), \text{ and}$$

$$\hat{\zeta}\cdot\nabla\times\underset{\sim}{B} = 0 \text{ for all } (m/n),\ (m/n) \neq (0/0)$$

For a constant voltage boundary condition, we let

$$\hat{\zeta}\cdot\nabla\times\underset{\sim}{B} = \frac{E_{\hat{\zeta}_{wall}}}{\eta_{wall}} \text{ for } (m/n) = (0/0),$$

whereas in the constant current case,

$$B_{\theta_{wall}} = B_\theta(\, r_{I+1/2}\, ;0/0) = \text{constant.}$$

Note that in the first case, $E_{\zeta_{wall}}$ is a prescribed function of time,but in the latter, it is implicitly determined by the condition on B_θ.

The pressure field satisfies the Neumann condition

$$\frac{\partial p}{\partial r} = \hat{r}\cdot(-\nabla\cdot \underset{\sim}{\underset{\sim}{u}}\underset{\sim}{u} + \underset{\sim}{J}\times\underset{\sim}{B}), \tag{26}$$

which is consistent with the vanishing of u_r at the wall.

3.5 Numerical Stability

Linearizing Eqs.(2-7) about a uniform state and Fourier analyzing the resulting equations, we obtain

$$\frac{\partial \underset{\sim}{u}}{\partial t} = i(\underset{\sim}{k}\cdot \underset{\sim}{B}_o)\underset{\sim}{B}$$

$$\frac{\partial \underset{\sim}{B}}{\partial t} = i(\underset{\sim}{k}\cdot \underset{\sim}{B}_o)\underset{\sim}{u},$$

where $\underset{\sim}{B}_o$ is the equilibrium field. For these equations, the predictor-corrector scheme of Eqs.(9-12) is linearly stable if

$$\delta t|\underset{\sim}{k}\cdot \underset{\sim}{B}_o| < 1. \tag{27}$$

Because the fluid is incompressible, maximum step-size is independent of the radial mesh size δr. The maximum stable time step of a corresponding compressible calculation is determined by the compressional Alfven time, which, in our units, would give the approximate Courant condition

$$\frac{\delta t\, B_o}{\delta x} < 1,$$

where $\delta x = \min\{\delta r, \frac{2\pi\delta r}{M}\}$, and M is the largest poloidal mode number included in the calculations. For a typical tokamak q-profile, $|\underset{\sim}{k}\cdot\underset{\sim}{B}_o|_{max} \sim O(M)$. Thus,

$$\frac{\delta t_{incomp}}{\delta t_{comp}} \sim I,$$

where I is the number of radial mesh points, and δt_{comp}, δt_{incomp} are maximum time steps in compressible, and incompressible fluid calculations, respectively. Since in general we have $I \sim O(10^2)$, the saving in computer time is substantial for an incompressible calculation.

Note that the stability condition of Eq.(27) does not involve resistivity either, since the resistive part of the induction equation is treated implicitly.

Linear numerical stability does not guarantee the stability of the code in highly nonlinear calculations, where we are sometimes forced to use a time step smaller than allowed by Eq.(27). We have devised the following ad hoc scheme which keeps δt near an optimum level throughout a calculation.

One of the earliest symptoms of a developing numerical instability in our code is that the Fourier coefficients exhibit temporal, as well as spatial, oscillations . In particular, $B_r(r,t;m/n)$, where (m/n) is that mode for which $|\underset{\sim}{k}\cdot\underset{\sim}{B}_o|$ is maximum, shows the following temporal behavior:

$$B_r(r^*,t;m/n) \sim a(t)\sin\frac{2\pi t}{\tau},\ r^*=(r_1,\text{or } r_{I-1}). \qquad (28)$$

As the instability develops, the period τ becomes shorter, while the amplitude a(t) grows. Thus, to be able to detect an instability before it becomes harmful, we continuously monitor $B_r(r^*,t;m/n)$,and reduce δt when τ drops below $c_1\delta t$. Similarly δt is increased when $\tau > c_2\delta t$, where the parameters c_1 and c_2 are usually set to 3 and 12,respectively. This algorithm keeps the code running with a time step just below the instability level and has proved to be superior to others we have tested.

4. SAMPLE CALCULATONS

4.1 m=1 Resistive Tearing Mode

In the cylindrical approximation, tokamak plasmas become unstable to an m=1 mode whenever the safety factor drops below one on the axis. In the ideal MHD limit,the mode saturates at a moderate amplitude after the plasma reaches a helical equilibrium with a singular current sheet at the q=1 rational surface [14,15].In the presence of resistivity, this current singularity is resolved by tearing and reconnection of the field lines, which leads to the formation of a large m=1 island. In Kadomtsev's heuristic analysis of the reconnection process [16],this island eventually squeezes out the original magnetic axis,flattening the current profile and raising q on axis to unity. Calculations of Waddell, et. al., essentially confirmed Kadomtsev's analysis [11]. These calculations were done in the

large aspect ratio limit, where the ideal mode is neutral. Using an aspect ratio of 100 ($\varepsilon=10^{-2}$), we reproduce their results, although with $\varepsilon=1/3$, our results are qualitatively different.

a) Equilibrium, and Linear Calculations

The equilibrium current density is given by [11]

$$J_{\zeta_o}(r) = \frac{J_o}{[1+(r/r_{ch})^2]^2}, \tag{29}$$

where r_{ch} is the current channel width normalized to minor radius. With $J_o=2.22$, and $r_{ch}=0.6$, we have $q_o=0.9$, $q_{wall} = 3.4$, and r_s, the radius of the q=1 surface, is at 0.2.

The resistivity profile is determined by

$$S(r) = S_s \frac{J_{\zeta_o}(r)}{J_{\zeta_o}(r_s)}, \tag{30}$$

where $S_s=5.0\times 10^4$.

With this equilibrium, the linear growth rate of the m=1 mode as a function of the aspect ratio is shown in Table I.

Linear theory, which is valid only in the large aspect ratio and large S limit, predicts for the same parameters a growth rate of 2.71×10^{-2}. As expected, the difference between theoretical and numerical growth rates becomes less as S is increased, as shown in Table II.

For the run with $S=10^8$, for which the perturbed current density is shown if Fig. 2,the grid spacing was 2.5×10^{-4} near the singular layer.

b) Nonlinear Calculations

Nonlinear evolution of the mode is investigated for two different aspect ratios using 20 Fourier harmonics. For $\varepsilon=10^{-2}$, we reproduce the results of Waddell, et. al. [11], as shown in Figs. (3,4), but for $\varepsilon=1/3$, our results are qualitatively and quantitatively different. In this case, the vortex structure characteristic of the flow field for an m=1 mode goes through many reversals in sign during the evolution of the mode. In Figs.(5,6),the velocity field and the helical flux contours are shown at different times for this nonlinear run. At t=290, we observe the usual m=1 island, and the counter rotating vortices carrying the magnetic axis towards the x-point. Figs. 5b,c,and d show the various stages of the first reversal. First, two more vortices in opposite directions to the first two appear. They later dominate and convect the plasma away from the x-point, towards the center of the column. During this inverse reconnection (Fig. 6d), a new magnetic axis forms; tearing and reconnection at the x-point contribute to the formation of flux surfaces around this new axis, in contrast to the original convection process that fed flux into the m=1 island from the magnetic axis. By t=450,the convection pattern resumes its

initial direction. This reversal is repeated a few more times before the direction of the flow pattern becomes steady. However,the mode seems to saturate without total reconnection, as the island is still visible at $t=1.23\times10^3$ (Fig. 6e).A plot of the kinetic energy for this run is shown in Fig. 7. The final level is characteristic of a steady flow associated with the saturated state.

4.2 Self Reversal in a Reversed Field Pinch

A reversed field pinch (RFP) is a device that carries a toroidal current and an externally induced toroidal field [17]. It differs from a tokamak mainly in that the toroidal and poloidal fields are of comparable magnitude, and the safety facter q is less than unity everywhere in the plasma. Ideal MHD stability is maintained by a combination of high magnetic shear and a close fitting conducting wall.

When the pinch parameter $\theta \equiv B_{\theta_{wall}}/\langle B_\zeta \rangle_V$ is large enough, where $\langle B_\zeta \rangle_V$ is the volume averaged toroidal field, such devices, after going through an unstable phase, exhibit a quiescent state in which the toroidal field is reversed near the wall [18]. We are currently studying this self-reversal phenomenon and briefly discuss some preliminary results here.

The calculations start from an initial equilibrium in which the plasma has been compressed away from the wall by the toroidal current. The current and q-profile for the zero-β equilibrium we will discuss are shown in Fig. 8. Initial value of the pinch parameter is 1.98, and $S = 5\times10^3$, constant in space and time.

The most unstable modes for this equilibrium are $m/n=1/2$ ($m=1, k_z=2$), and $1/3$ ($m=1$, and $k_z=3$), for which the growth rates are 9.42×10^{-1}, and 2.70×10^{-1}, respectively. Instead of including in the calculations all modes $(m/n), -M\leq m\leq M$, $0\leq n\leq N$, where M,N are some cutoff mode numbers, modes are selected on the basis of a mode pyramid generated by the nonlinear interaction of $m/n=1/2$, and $1/3$ [9]. Typically about 60 modes are used in our calculations.

Kinetic energy history from a typical run is shown in Fig. 9. Initial exponential growth, and subsequent oscillations are mainly due to the (1/2) mode. Since the $q=1/2$ surface is not present in the plasma initially, and $B_r=0$ on the wall, this mode saturates without any reconnection. The oscillatory behavior is caused by its initial overshoot and lack of adequate viscous damping.

Sudden increase in the kinetic energy around $t=120$ is accompanied by a pronounced reversal of the axial field on the wall (Fig. 10). With no applied electric field at the boundary, the axial current decays, and reversal is lost by $t=300$. A plot of F vs. θ ,where $F \equiv B_{\zeta_w}/\langle B_\zeta \rangle_V$, is shown if Fig. 11.

Even after approximately 10^4 time steps,magnetic and velocity fields are divergence-free, as shown in Fig. 12, where we plot the time histories of the quantities

$$|| \nabla\cdot\underset{\sim}{u} || \equiv \max_{0<r<1} \sum_{m,n} \left| \frac{\partial}{r\partial r} r u_r + \frac{im}{r} u_\theta + \frac{in}{R_o} u_\zeta \right|, \tag{31}$$

and

$$|| \nabla\cdot\underset{\sim}{B} || \equiv \max_{0<r<1} \sum_{m,n} \left| \frac{\partial}{r\partial r} r B_r + \frac{im}{r} B_\theta + \frac{in}{R_o} B_\zeta \right|. \tag{32}$$

Note that since we set $\nabla\cdot\underset{\sim}{u}^{n+1} = 0$ at each time step, $||\nabla\cdot\underset{\sim}{u}||$ differs from zero only because of the roundoff and truncation errors that occur during that particular step, whereas the errors in $\nabla\cdot\underset{\sim}{B}$ accumulate over time, since the magnetic field only satisfies $\nabla\cdot\underset{\sim}{B}^{n+1} = \nabla\cdot\underset{\sim}{B}^{n}$. However, $||\nabla\cdot\underset{\sim}{B}||$ is still insignificant, even at the end of the run.

5. SUMMARY

A 3D initial value code that solves the nonlinear, resistive, incompressible magnetohydrodynamic equations in a cylindrical geometry has been developed. The equations are used in their nonreduced, primitive forms, thus making the code applicable to a variety of cases with finite β and aspect ratio. The numerical methods employed guarantee that both the velocity and the magnetic fields are exactly divergence-free. Incompressibility assumption and the implicit treatment of the diffusion terms eliminate restrictive stability conditions based on radial mesh size, and along with the use of Fourier expansions in the two periodic coordinates, produce an accurate and efficient code.

Preliminary simulation results have been obtained for both tokamak and RFP configurations. For a very large aspect ratio tokamak, results for the m=1 tearing mode reproduce theoretically predicted growth rates in the limit of large S. The nonlinear evolution of this mode in the large aspect ratio limit agrees with previous calculations based on reduced MHD equations. For small aspect ratio devices, the linear growth rate becomes much larger, approaching that of the ideal mode, and the nonlinear evolution is very different. Reconnection of the field lines inside the singular surface and the disappearance of the original magnetic axis is followed by an inverse reconnection process. A new m=1 island is generated, and the mode saturates, leaving the plasma with a helical deformation.

The simulation of an initially nonreversed screw pinch at moderate compression shows a self reversal of the axial field at the wall associated with a strong $m/n = 1/3$ instability. The resulting motion in the F,θ plane shows rapid relaxation toward a reversed field state, followed by a gradual relaxation due to resistive diffusion.

ACKNOWLEDGEMENTS

One of the authors (AYA) would like to thank Dr. Wonchull Park for his invaluable help and encouragement during the course of this work.

This work was supported by the United States Department of Energy, grant number DE-FG05-80ET-53088.

Table I. Linear growth rate of the m=1 mode as a function of the inverse aspect ratio, for $S=5.0\times10^{4}$.

ε	γ_{num}
1	7.64×10^{-2}
1/3	3.22×10^{-1}
1/10	2.02×10^{-2}
1/50	1.88×10^{-2}
1/100	1.87×10^{-2}
1/1000	1.87×10^{-2}

Table II. Linear growth rate of the m=1 mode as a function of S, for $\varepsilon=10^{-2}$.

S	γ_{num}	γ_{th}	% difference
5.0×10^{4}	1.87×10^{-2}	2.71×10^{-2}	45%
8.1×10^{5}	9.46×10^{-3}	1.07×10^{-2}	13%
8.1×10^{6}	4.69×10^{-3}	4.99×10^{-3}	6%
1.0×10^{8}	2.12×10^{-3}	2.15×10^{-3}	1%

REFERENCES

1. J. U. Brackbill, in "Methods in Computational Physics",(J. Killeen, Ed.), Vol. 16, p.1, Academic Press, New York, 1976.
2. D. Schnack,and J. Killeen, J. Comp. Phys. 35 (1980),110.
3. D. Gottlieb,and S. A. Orszag, "Numerical Analysis of Spectral Methods: Theory and Applications",Society for Industrial and Applied Mathematics, Philadelphia,1977.
4. H. R. Strauss, Phys. Fluids 20 (1977), 1354.
5. W. Park, D. A. Monticello, R. B. White, Bull. Am. Phys. Soc. 22 (1978),779.
6. H. R. Strauss, W. Park, D. A. Monticello, R. B. White, S. C. Jardin, M. S. Chance, A. M. M. Todd, and A. H. Glasser, Nucl. Fusion 5 (1980),638.
7. B. Carreras, H. R. Hicks, J. A. Holmes, B. V. Waddell,Phys. Fluids 23 (1980),1811.
8. B. Carreras, H. R. Hicks,and D. K. Lee, Phys. Fluids 24 (1981), 66.
9. H. R. Hicks,B. Carreras, J. A. Holmes, D. K. Lee, and B. V. Waddell, J. Comp. Phys. 44 (1981),46.
10. H. R. Strauss, Phys. Fluids 19 (1976),134.
11. B. V. Waddell, M. N. Rosenbluth, D. A. Monticello, and R. B. White, Nucl. Fusion 16 (1976),528.
12. F. H. Harlow, and J. E. Welch, Phys. Fluids 8 (1965),2182.
13. R. D. Richtmyer, and K. W. Morton,"Difference Methods for Initial Value Problems", 2nd ed., Interscience, New York, 1967.
14. M. N. Rosenbluth, R. Y. Dagazian, and P. H. Rutherford, Phys. Fluids 16, (1973),1894.
15. W. Park,D. A. Monticello, R. B. White,and S. C. Jardin, Nucl. Fusion 20, (1980),1181.

16. B. B. Kadomtsev, Sov. J. Plasma Phys. 1 (1975),389.

17. H. A. B. Bodin, and A. A. Newton, Nucl. Fusion 20,(1980),1255.

18. J. B. Taylor, Phys. Rev. Letters 33 (1974),1139.

FIGURE CAPTIONS

Fig. 1. The radial mesh is extended half a cell beyond the origin (r=0), and the conducting wall (r=1).

Fig. 2 a) Perturbed toroidal current density for the m=1 mode from a linear calculation with $\varepsilon=10^{-2}$, and $S=10^{8}$.

b) Tearing layer, where a plus sign (+) has been plotted at the value of J_ζ at each mesh point.

Fig. 3. Toroidal current density at various times during the nonlinear evolution of the m=1 mode in a tokamak with $\varepsilon=10^{-2}$. $S = 5\times10^{4}$ at the q=1 surface. a) t=486, b) t=586, c) t=636, d) t=956.

Fig. 4. Helical flux contours for the run of Fig. 3. The outermost flux surface shown is at r=0.25.

Fig. 5. Poloidal flow at various times during the nonlinear evolution of the m=1 mode in a tokamak with $\varepsilon=1/3$. $S = 5\times10^{4}$ at the q=1 surface. Only $r < 0.25$ part of the plane is shown.

Fig. 6. Helical flux contours for the run of Fig. 5. The outermost flux surface is at r=0.25.

Fig. 7. Kinetic energy history for the run of Fig. 5.

Fig. 8 a) Toroidal current density for the zero-β equilibrium used in the RFP self-reversal calculations.

b) Initial q profile for the RFP calculation.

Fig. 9. Kinetic energy history for the RFP self-reversal calculation.

Fig. 10. Value of the axial field on the wall for the RFP self-reversal calculation.

Fig. 11. F-θ diagram for the RFP calculation.

Fig.12 a) Time history of $||\nabla \cdot \underset{\sim}{u}||$, as defined by Eq. 31, for the RFP calculation.

b) $||\nabla \cdot \underset{\sim}{B}||$ history.

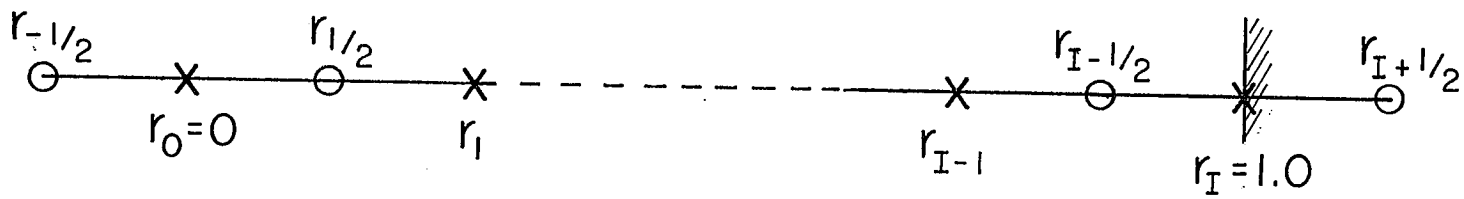

FIG. 1

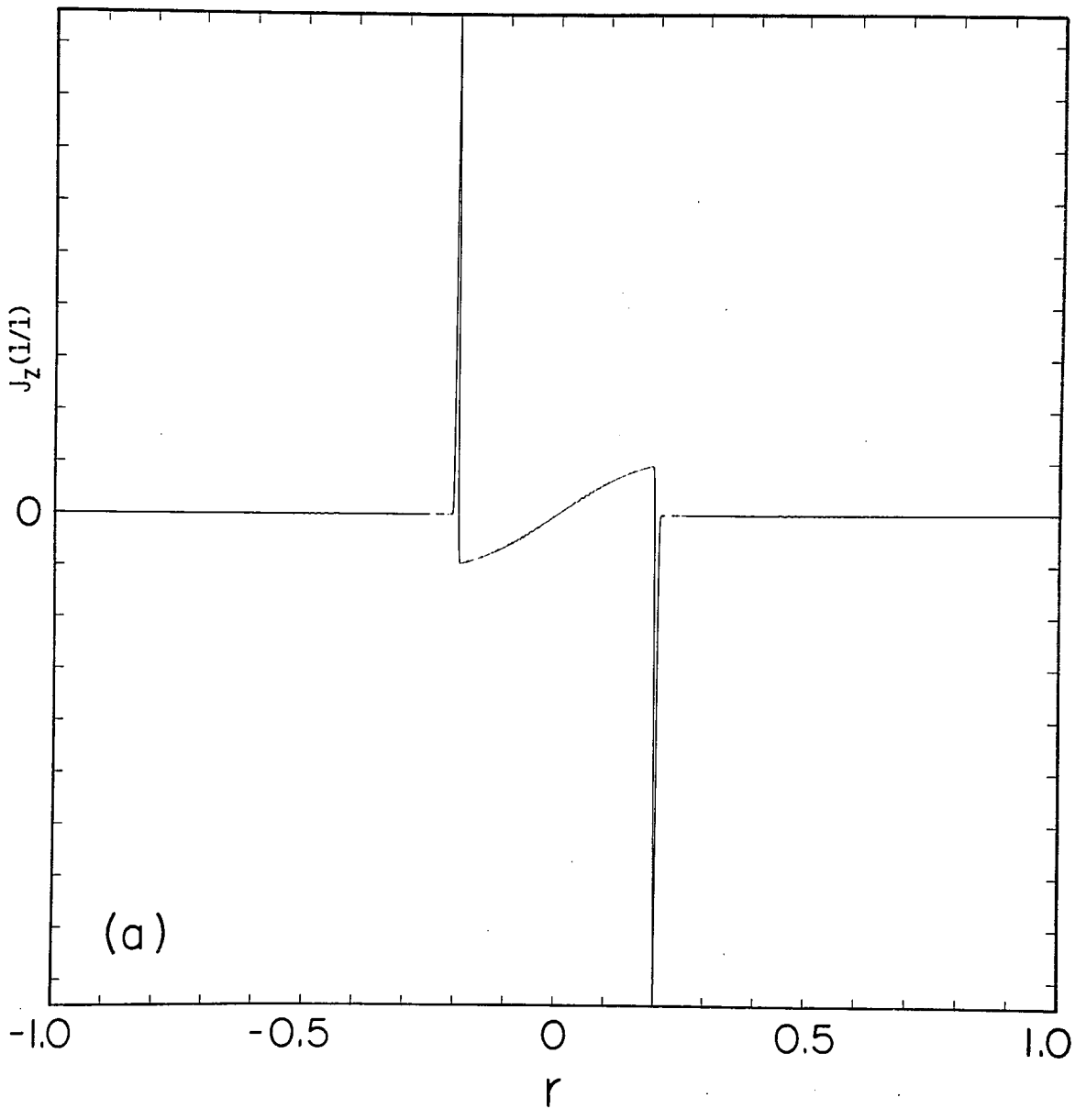

FIG. 2a

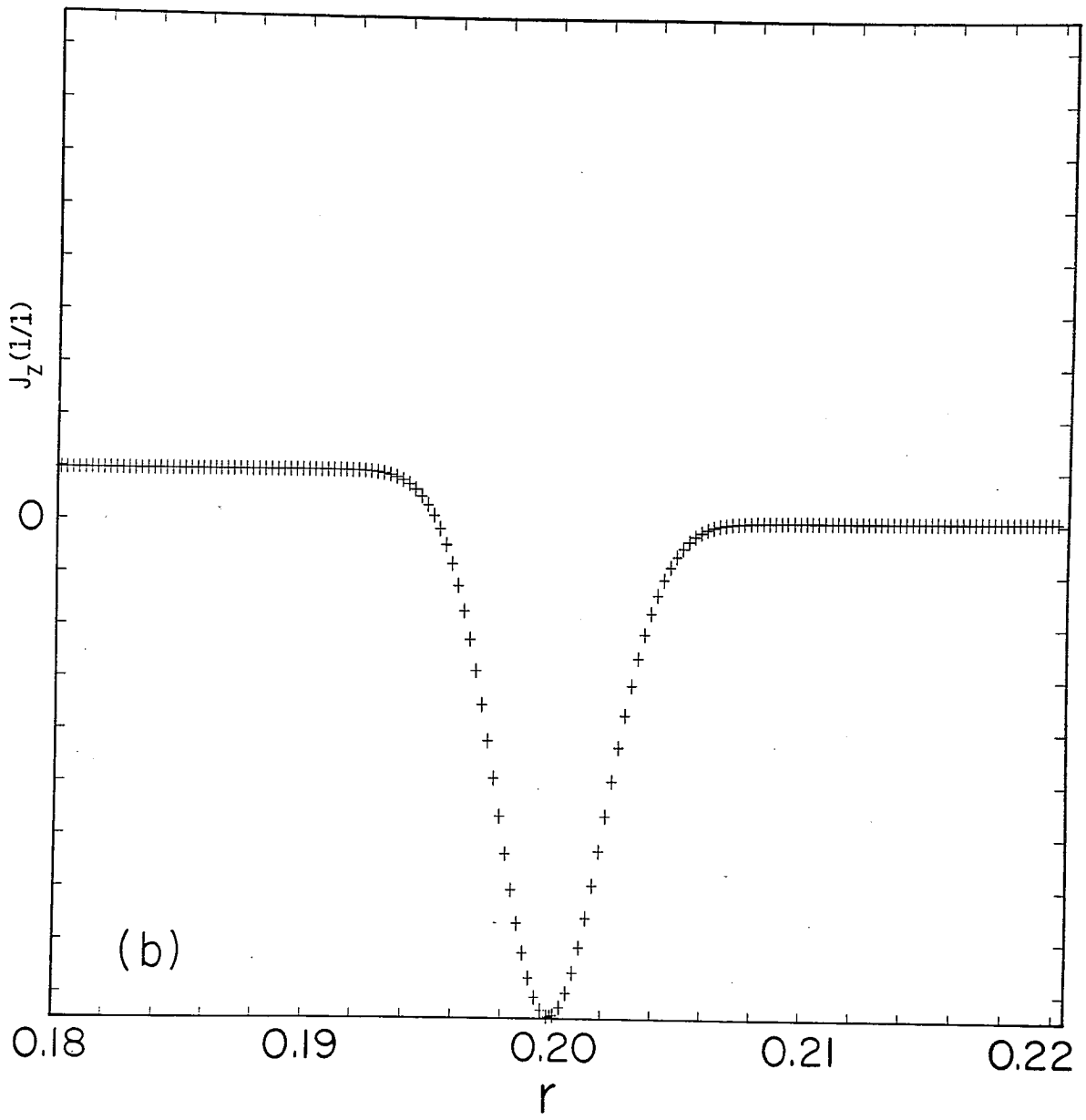

FIG. 2b

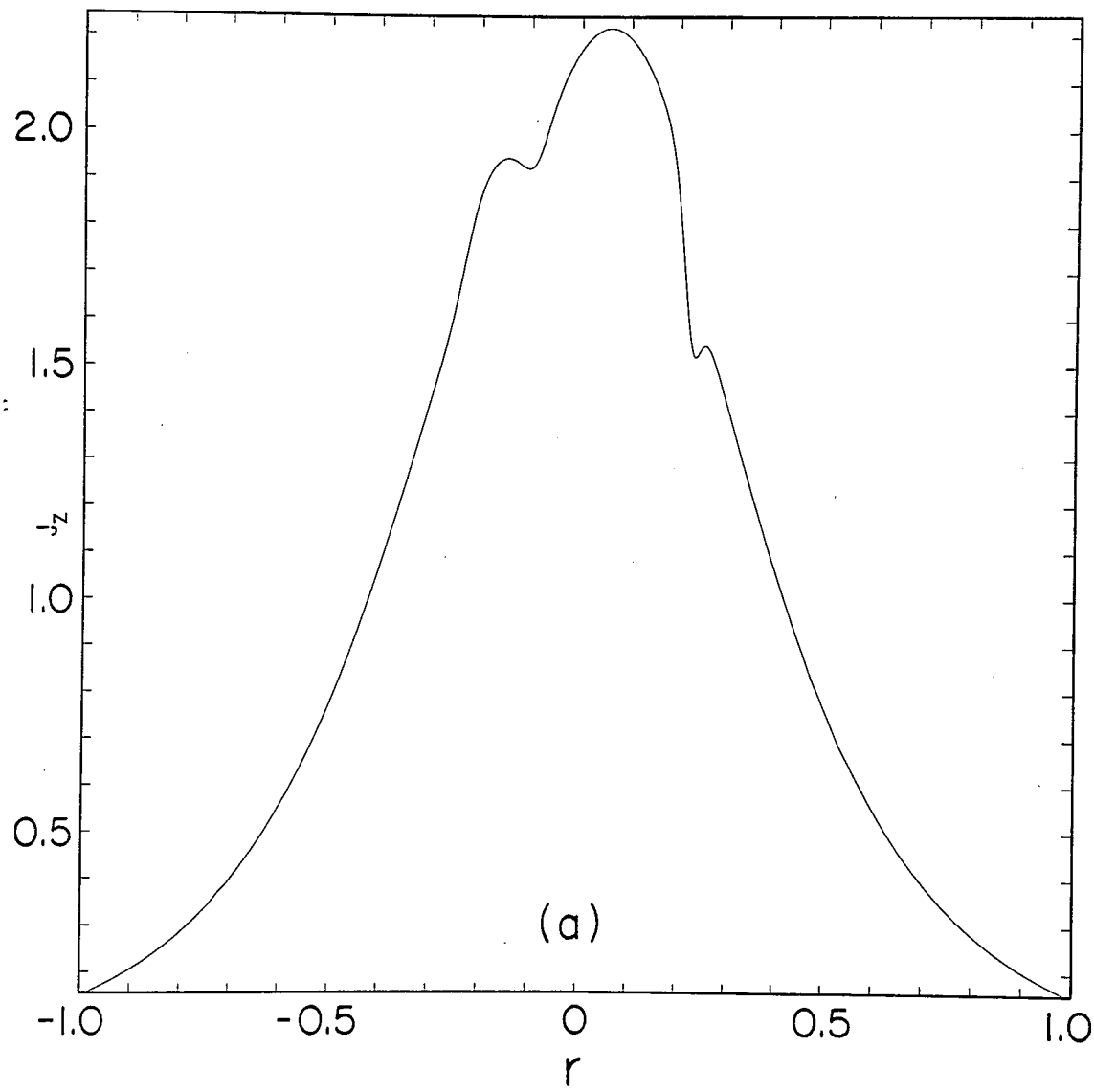

FIG. 3a

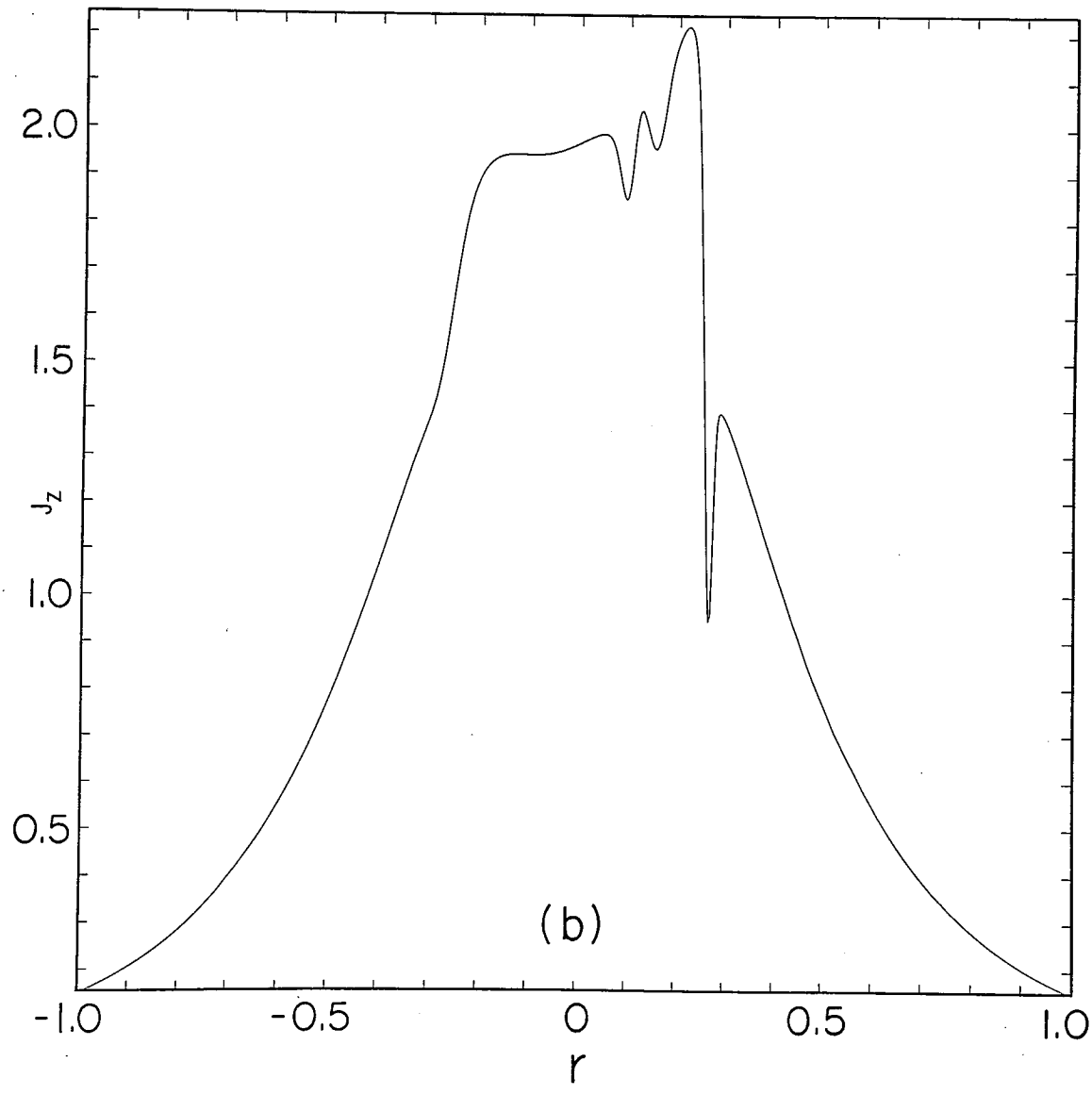

FIG. 3b

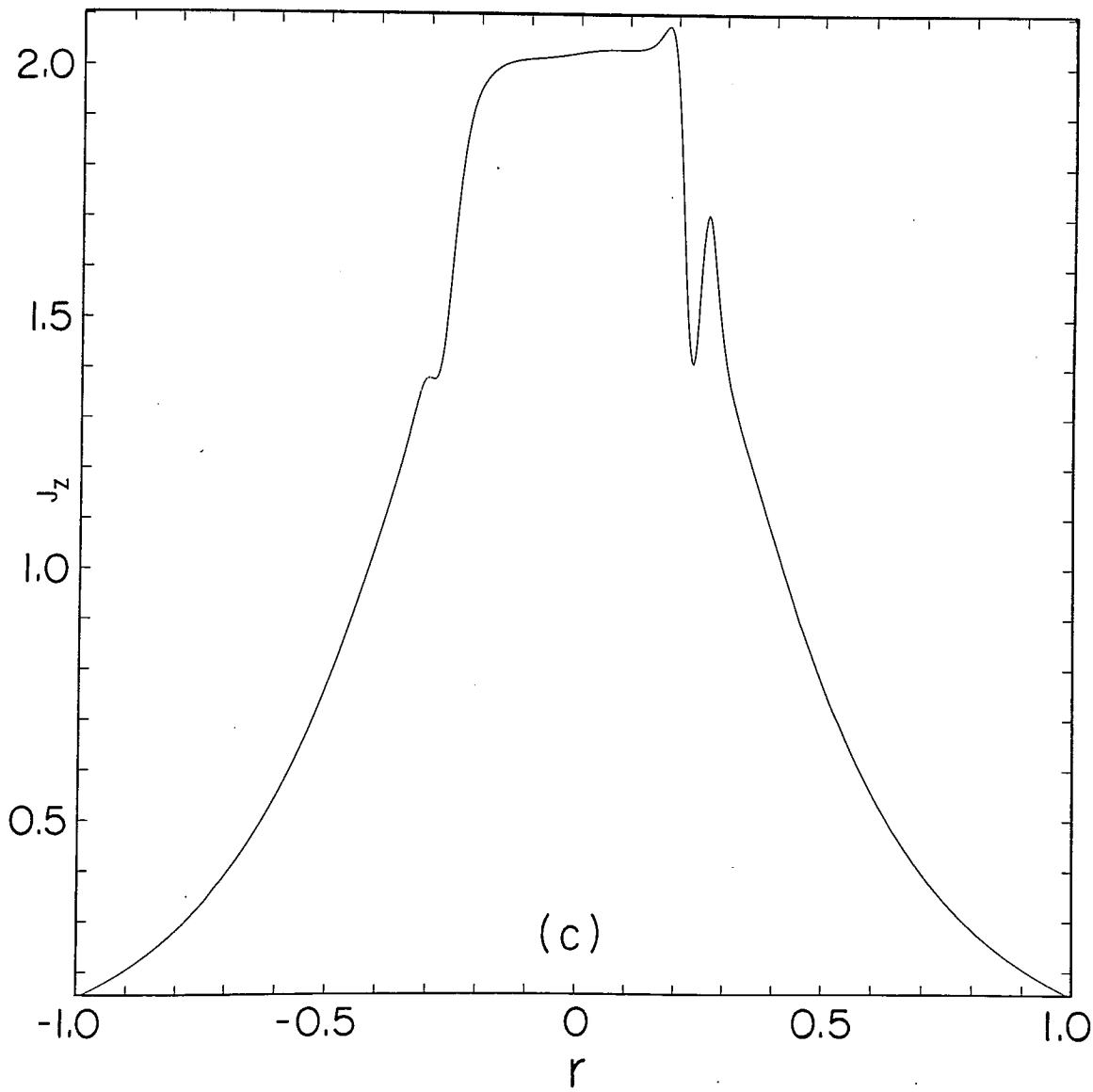

FIG. 3c

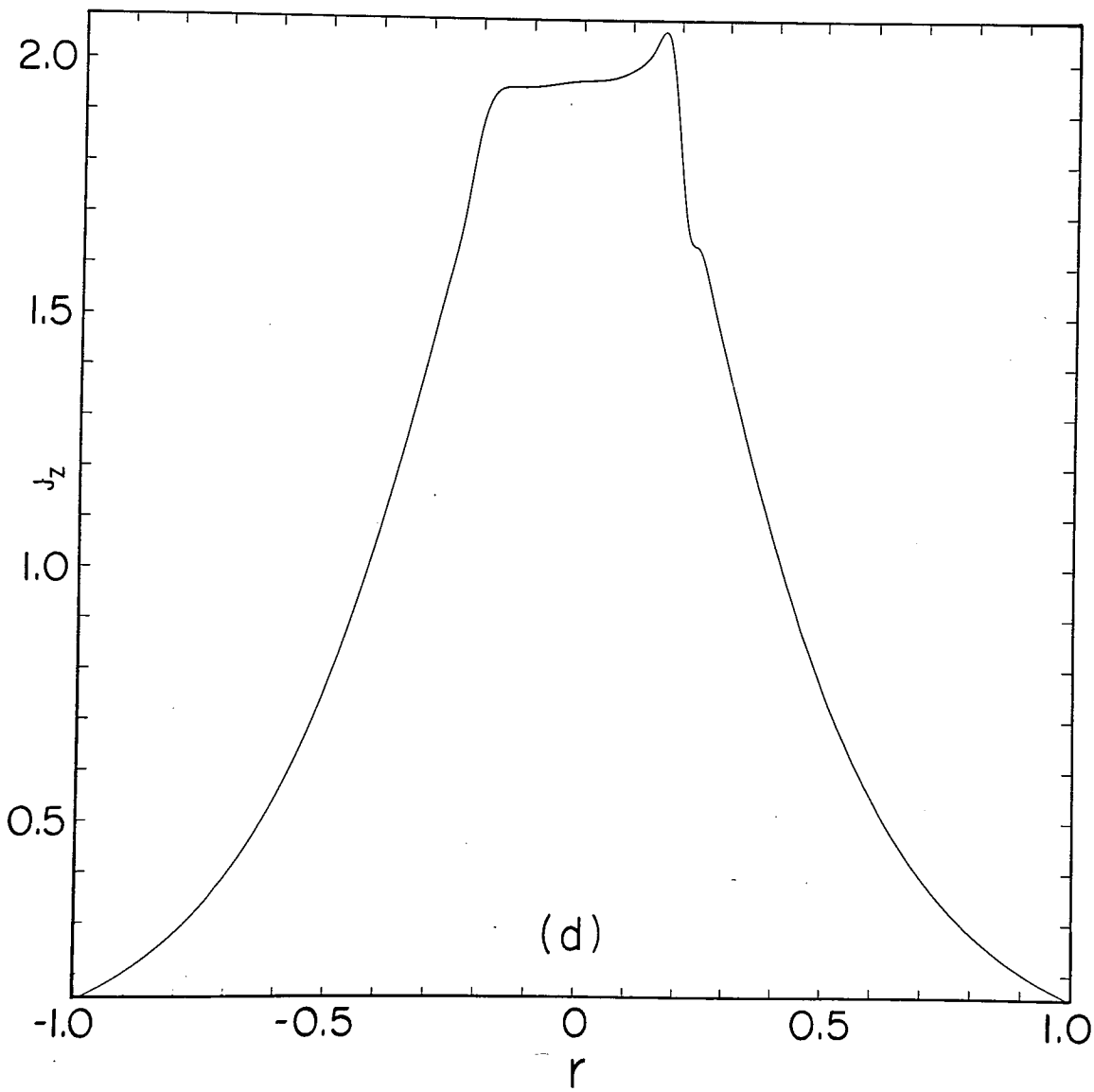

FIG. 3d

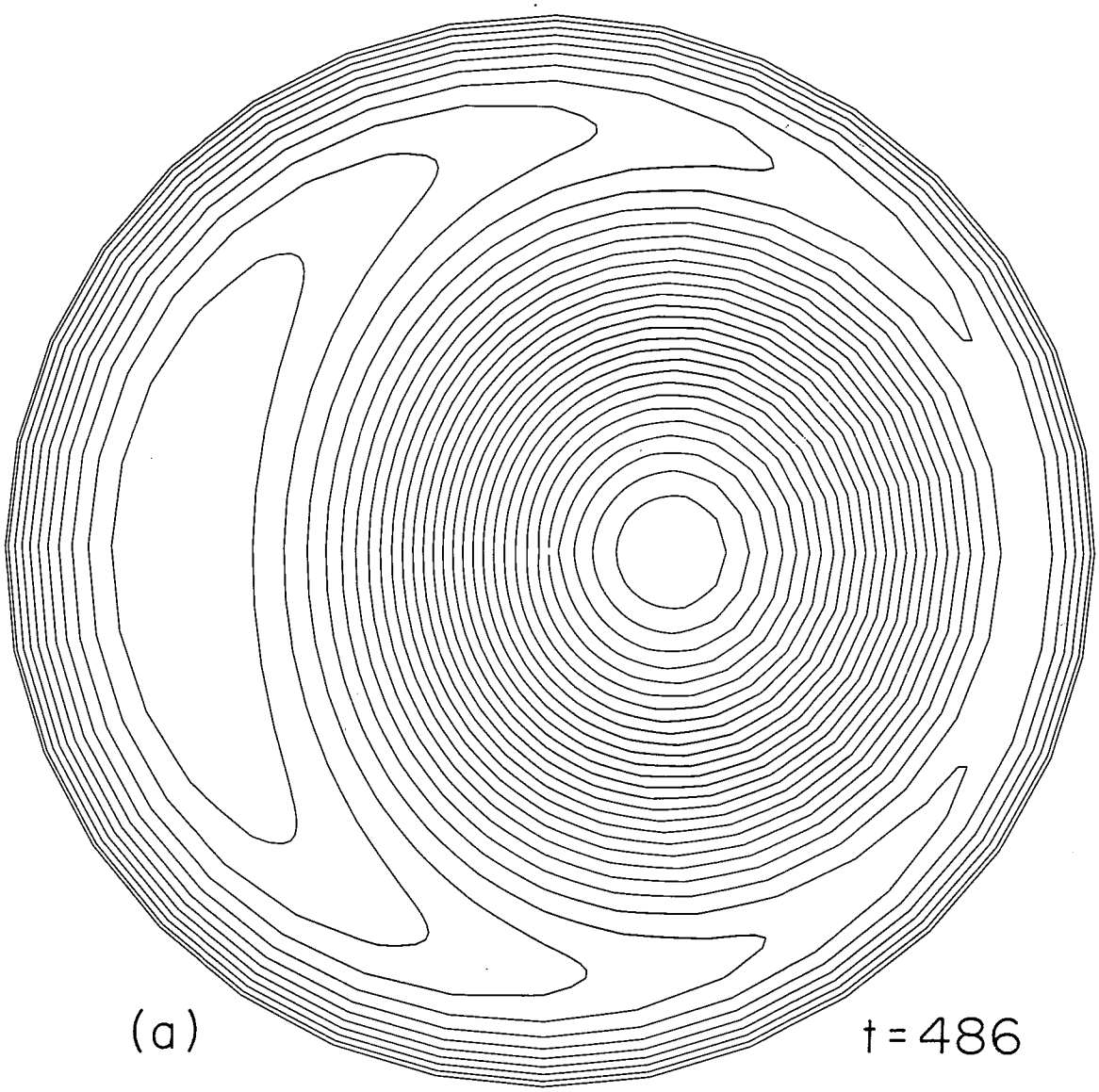

FIG. 4a

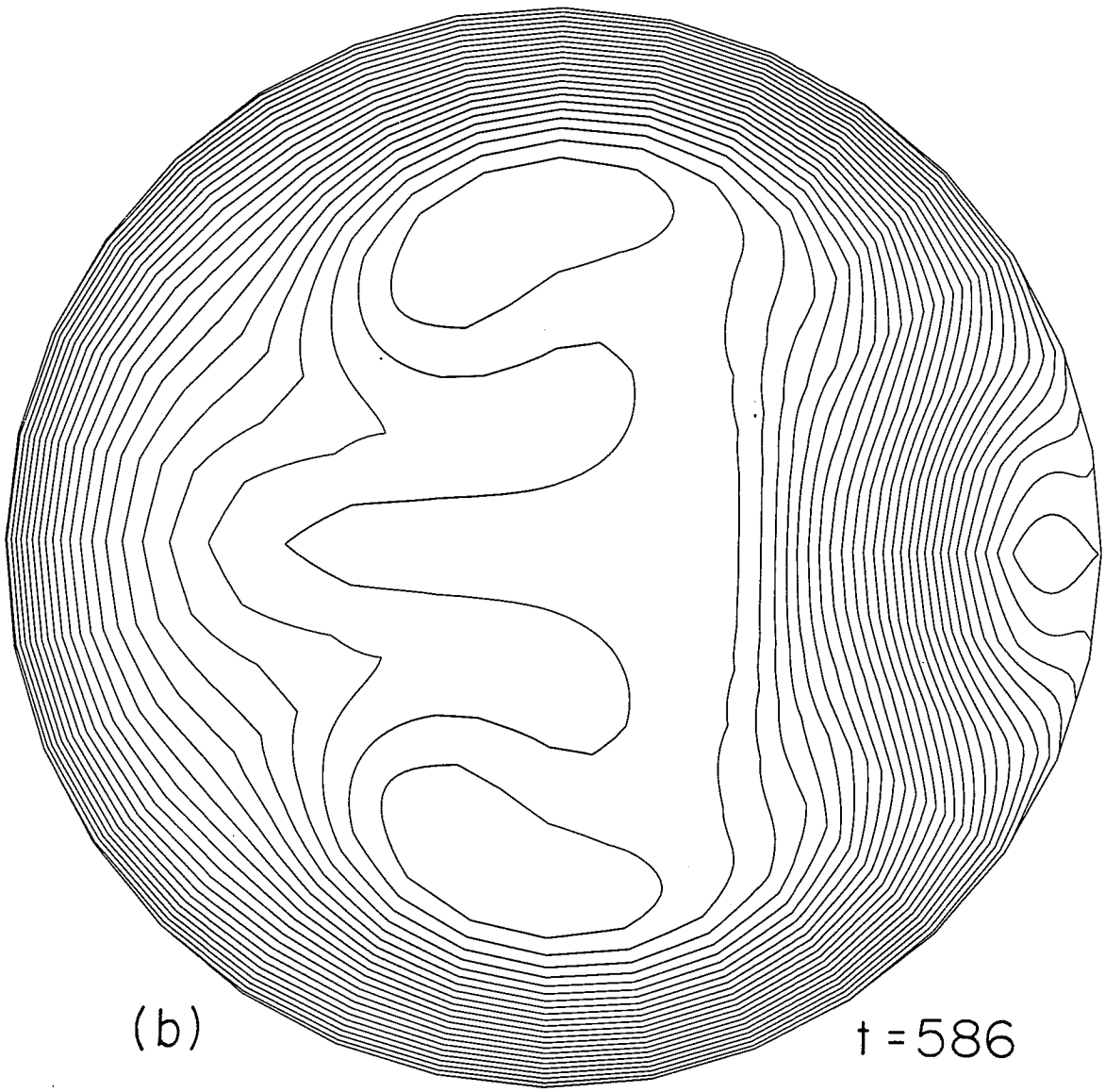

FIG. 4b

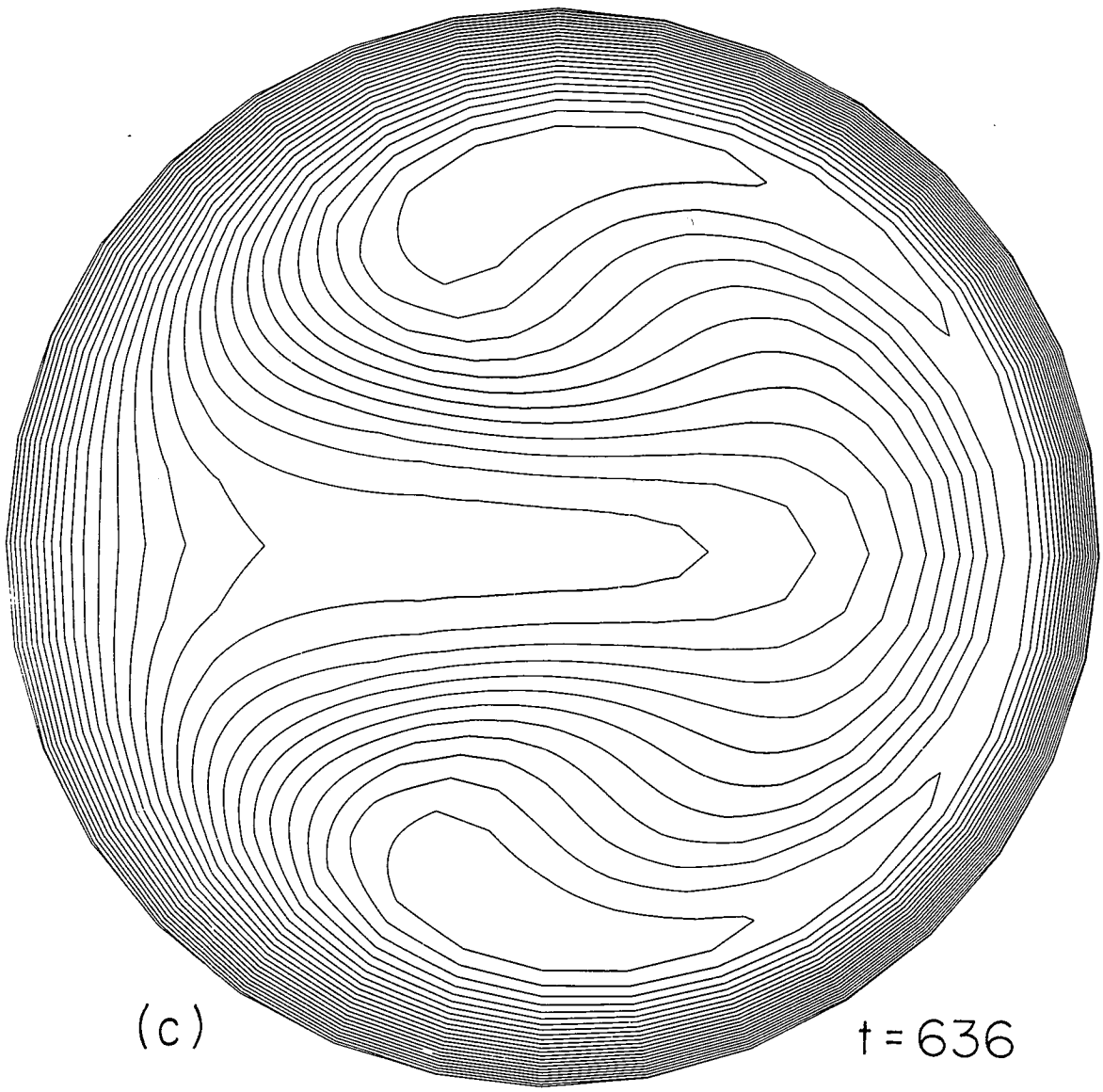

FIG. 4c

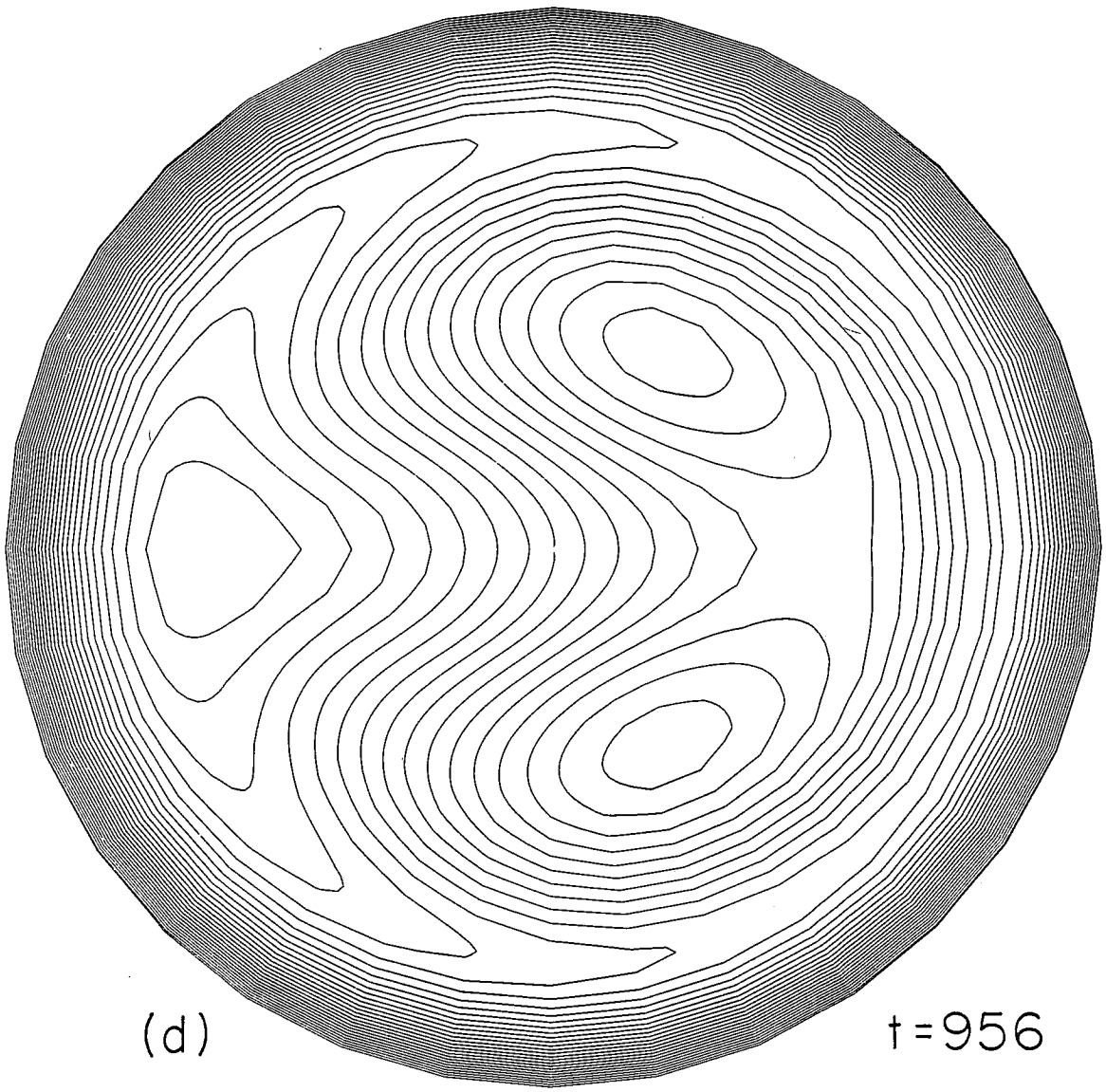

FIG. 4d

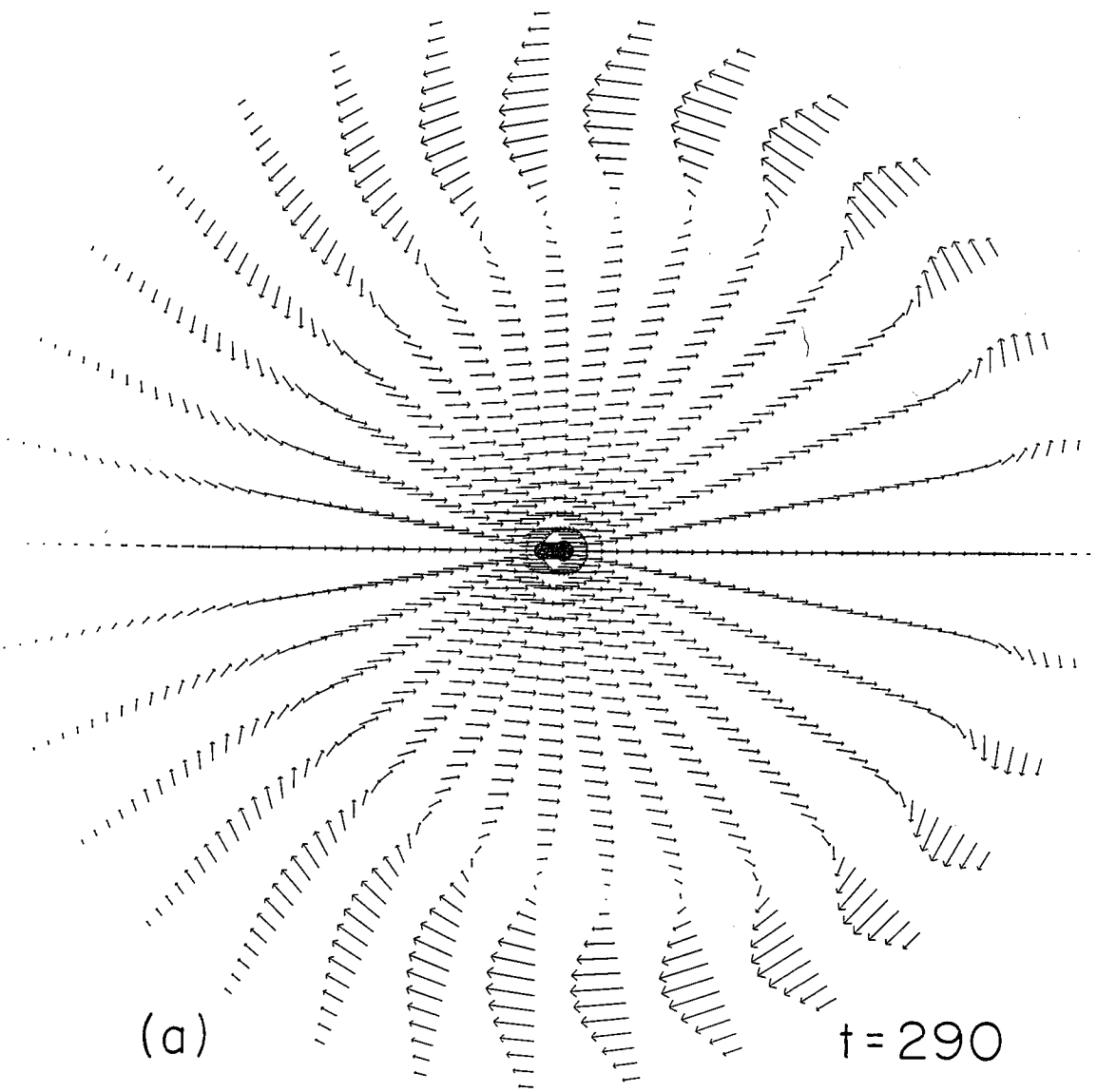

FIG. 5a

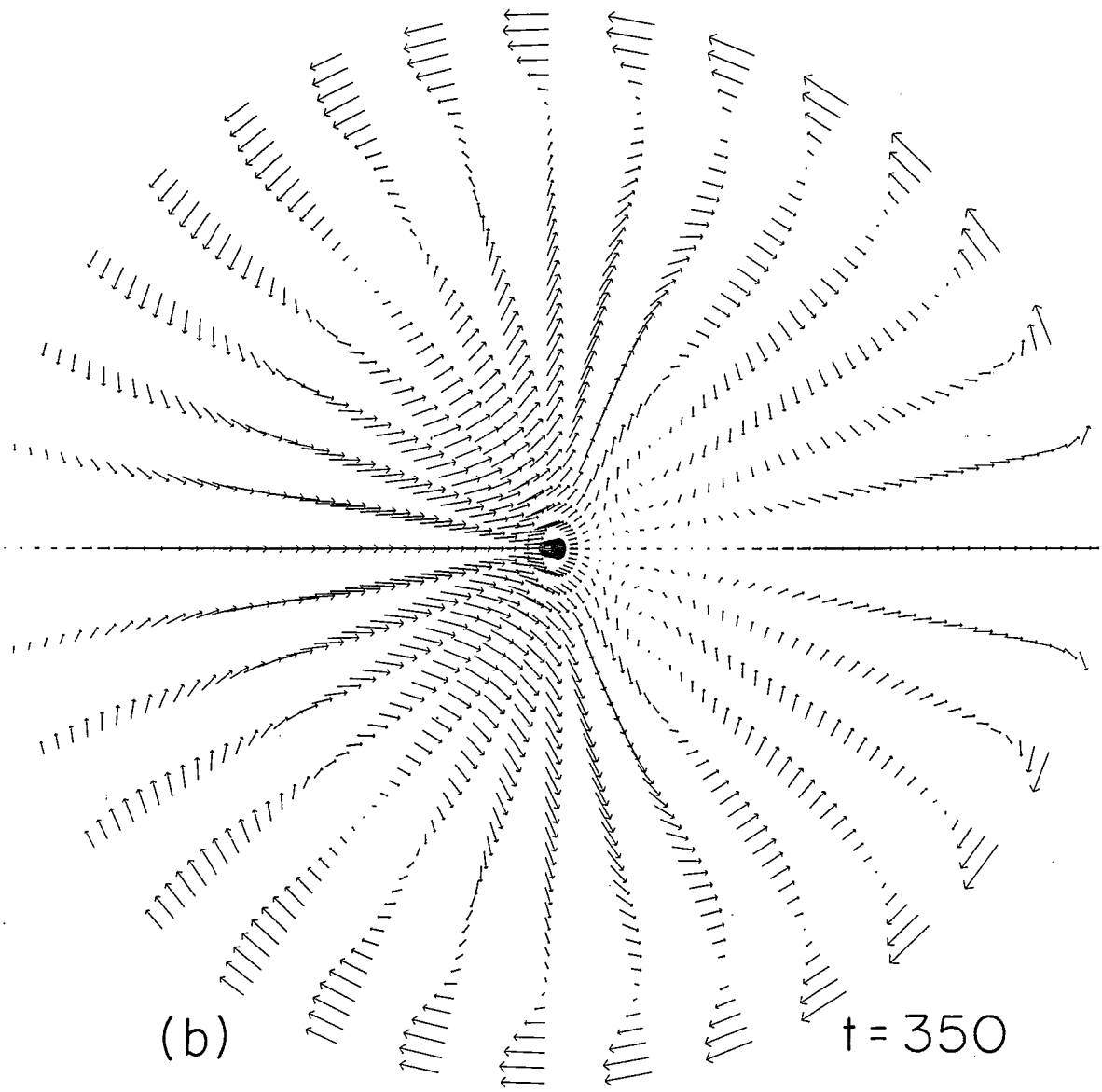

FIG. 5b

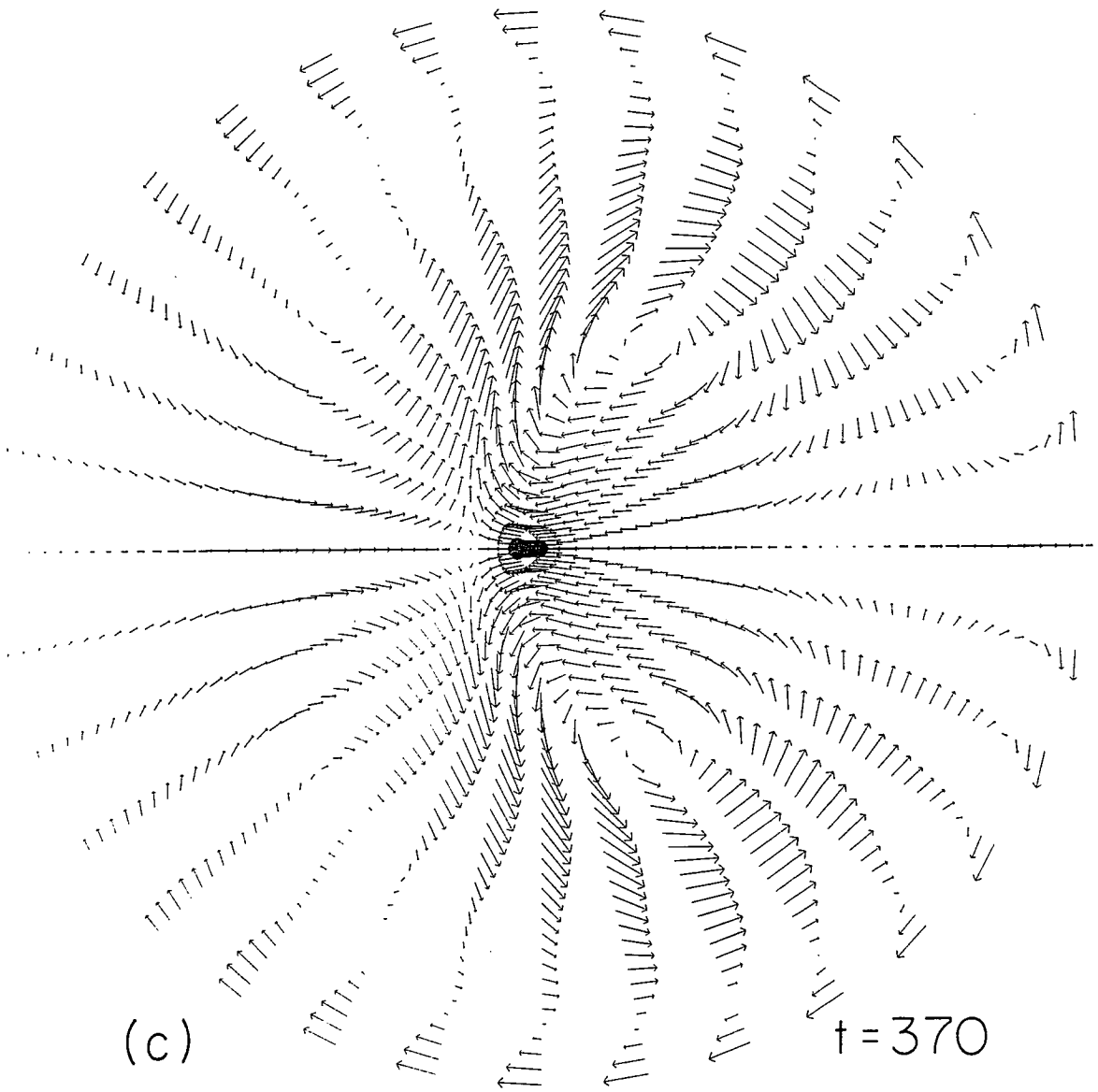

FIG. 5c

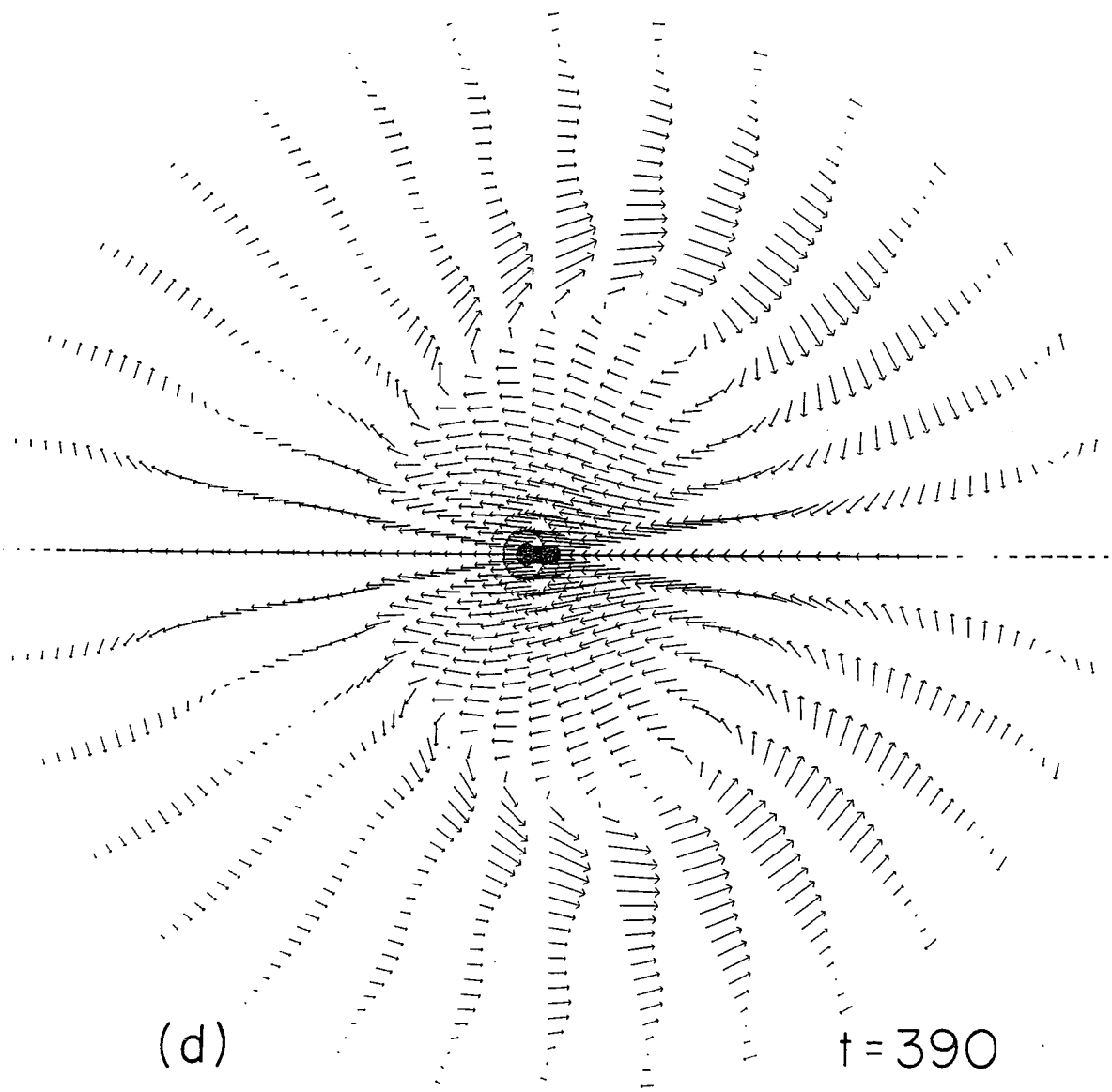

FIG. 5d

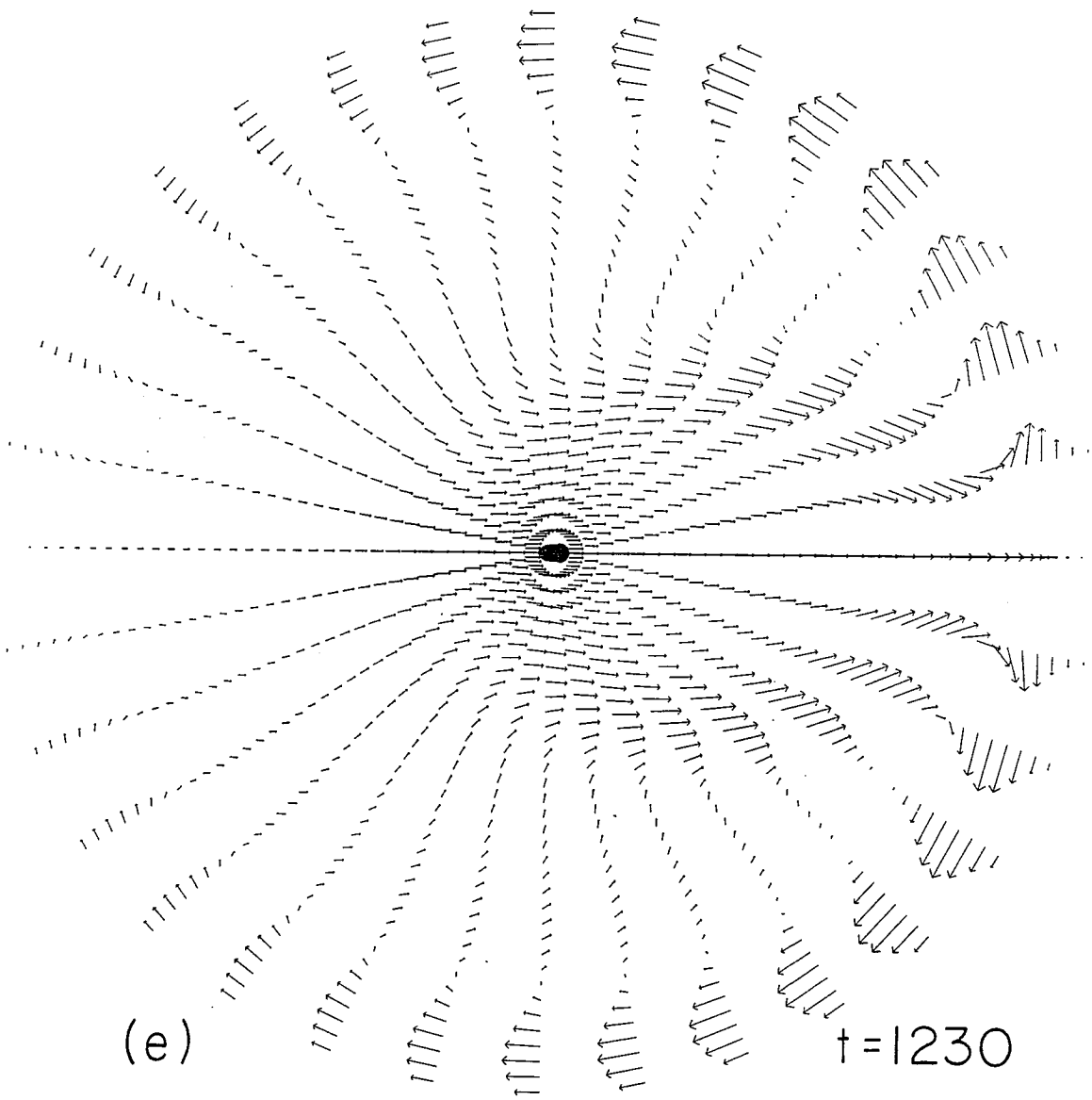

FIG. 5e

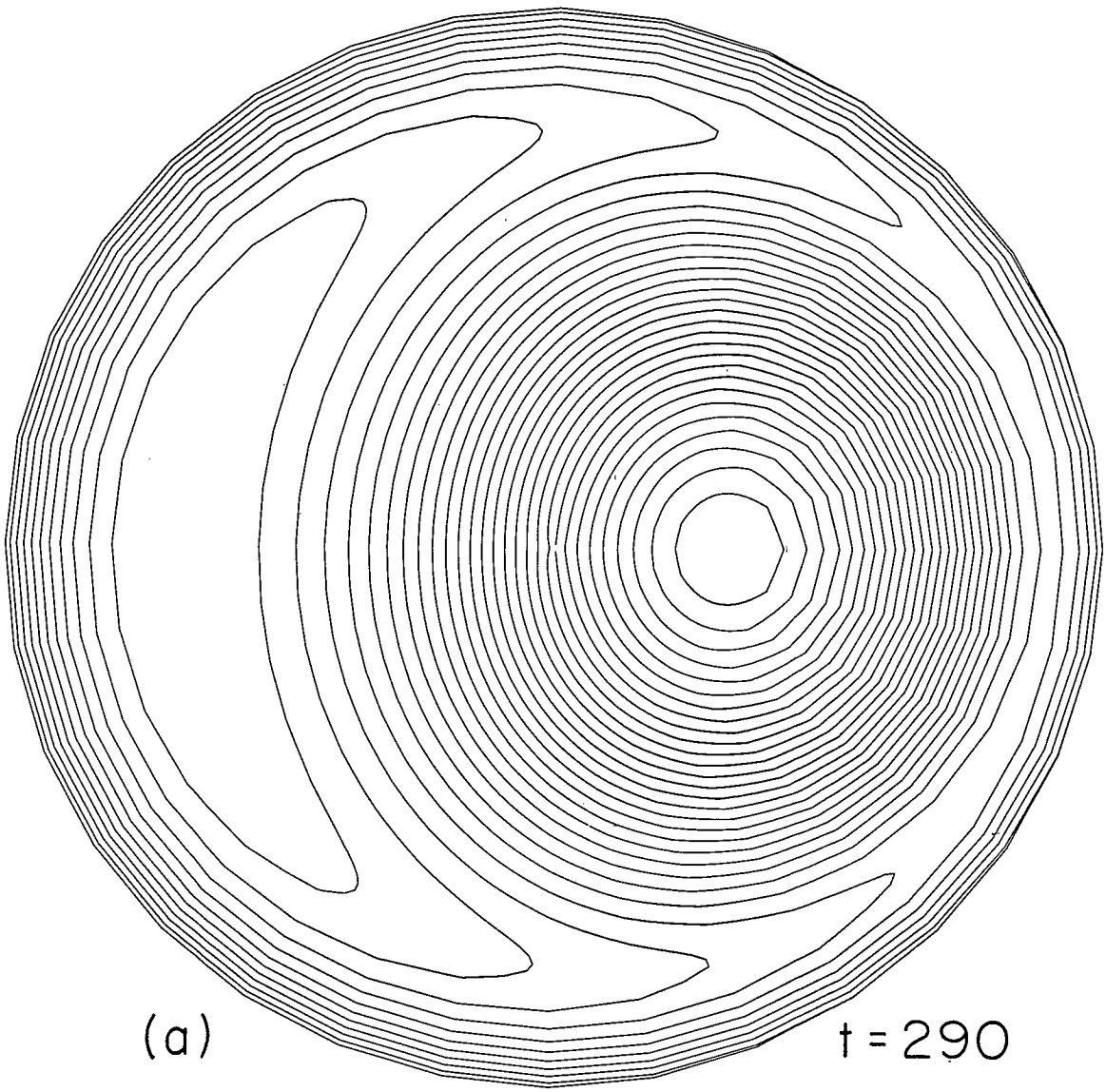

FIG. 6a

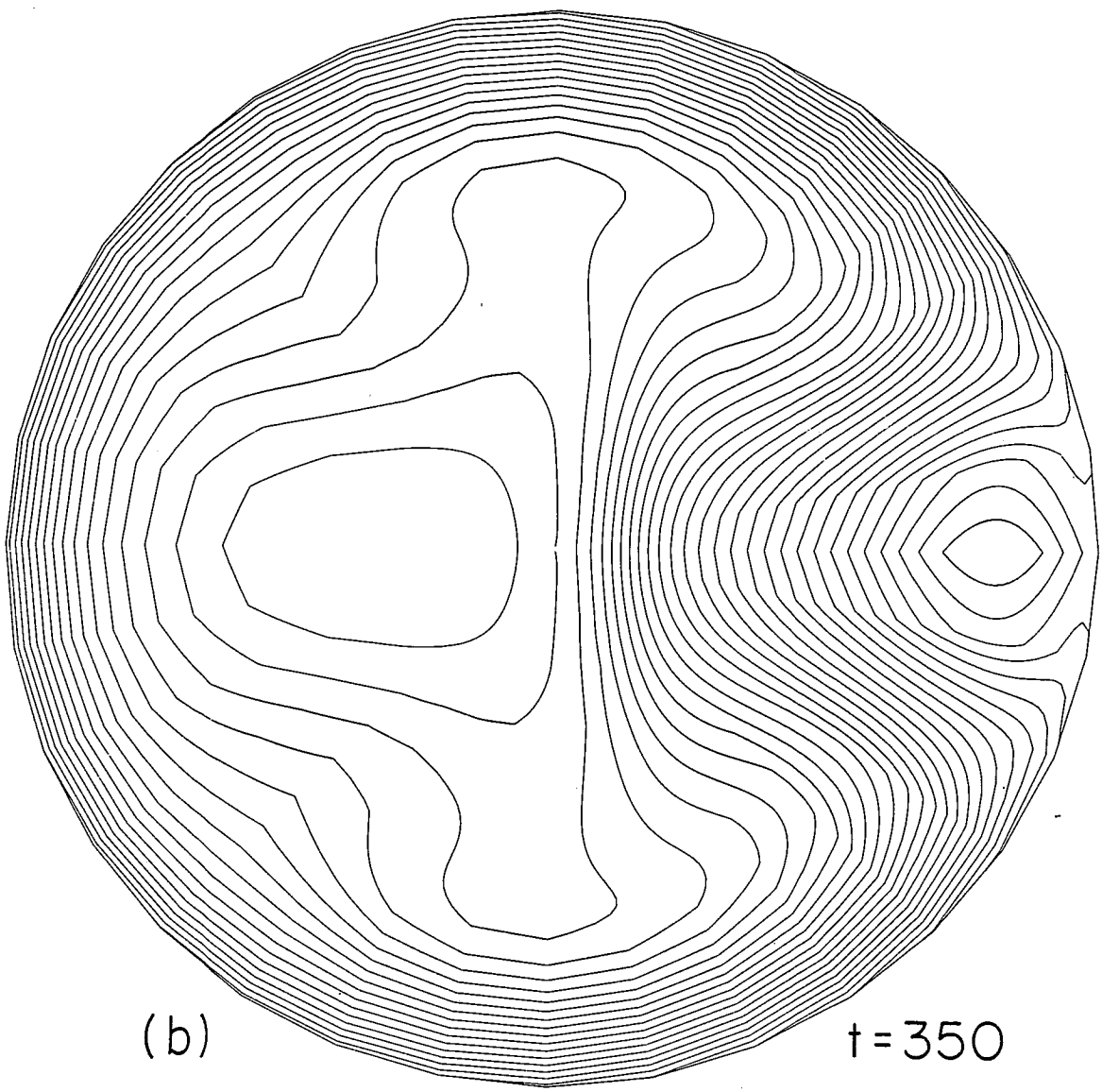

FIG. 6b

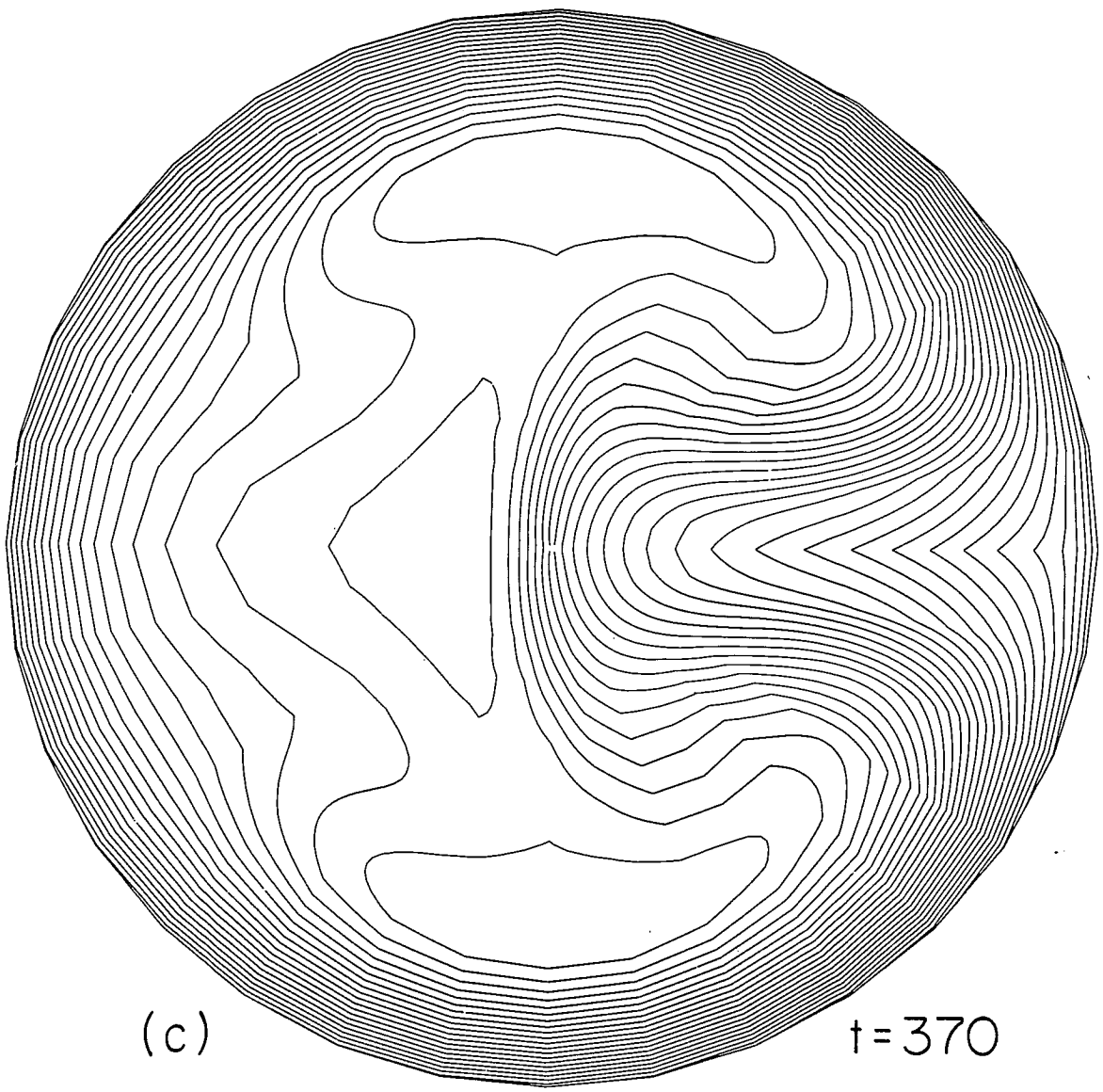

FIG. 6c

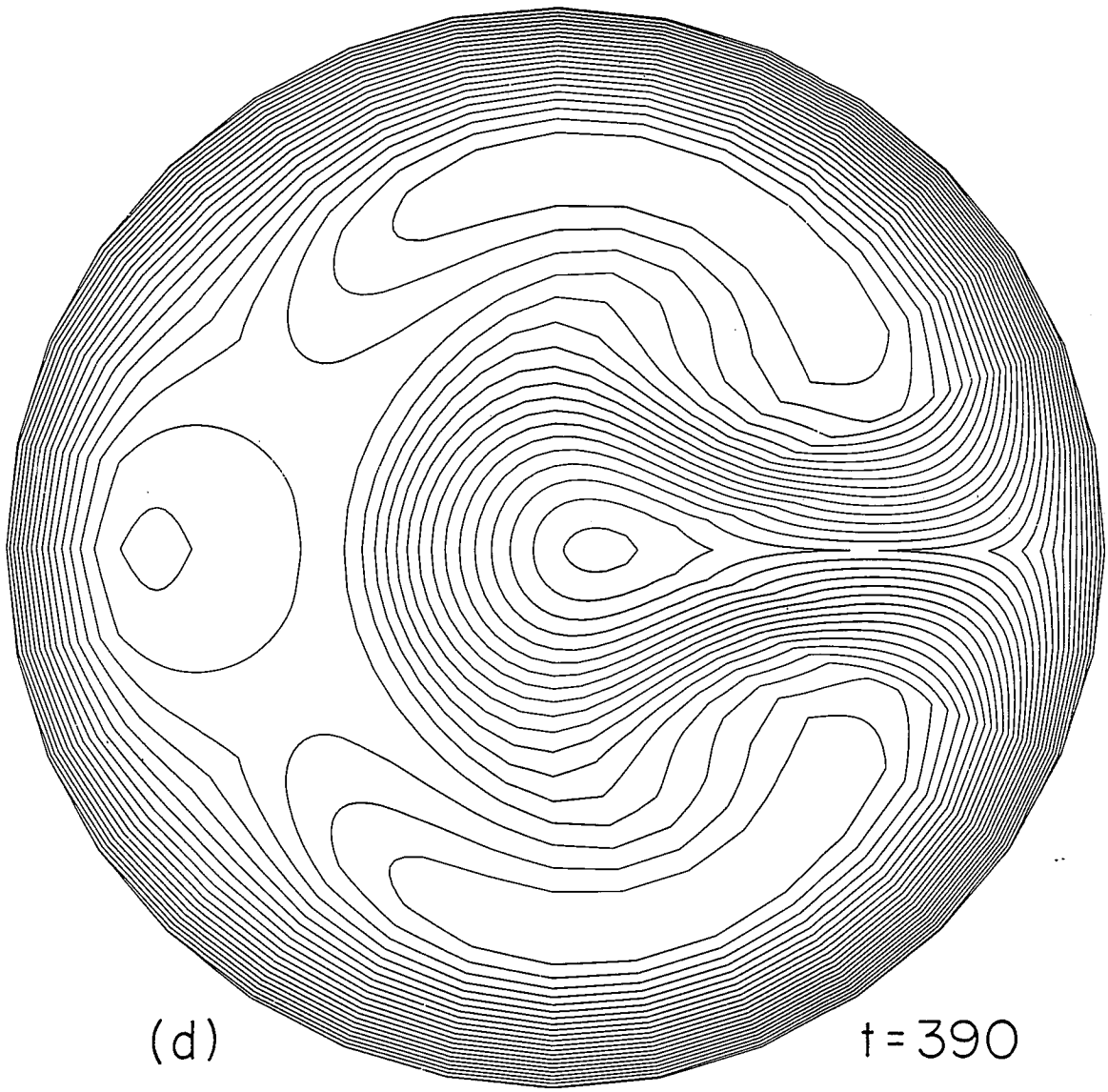

FIG. 6d

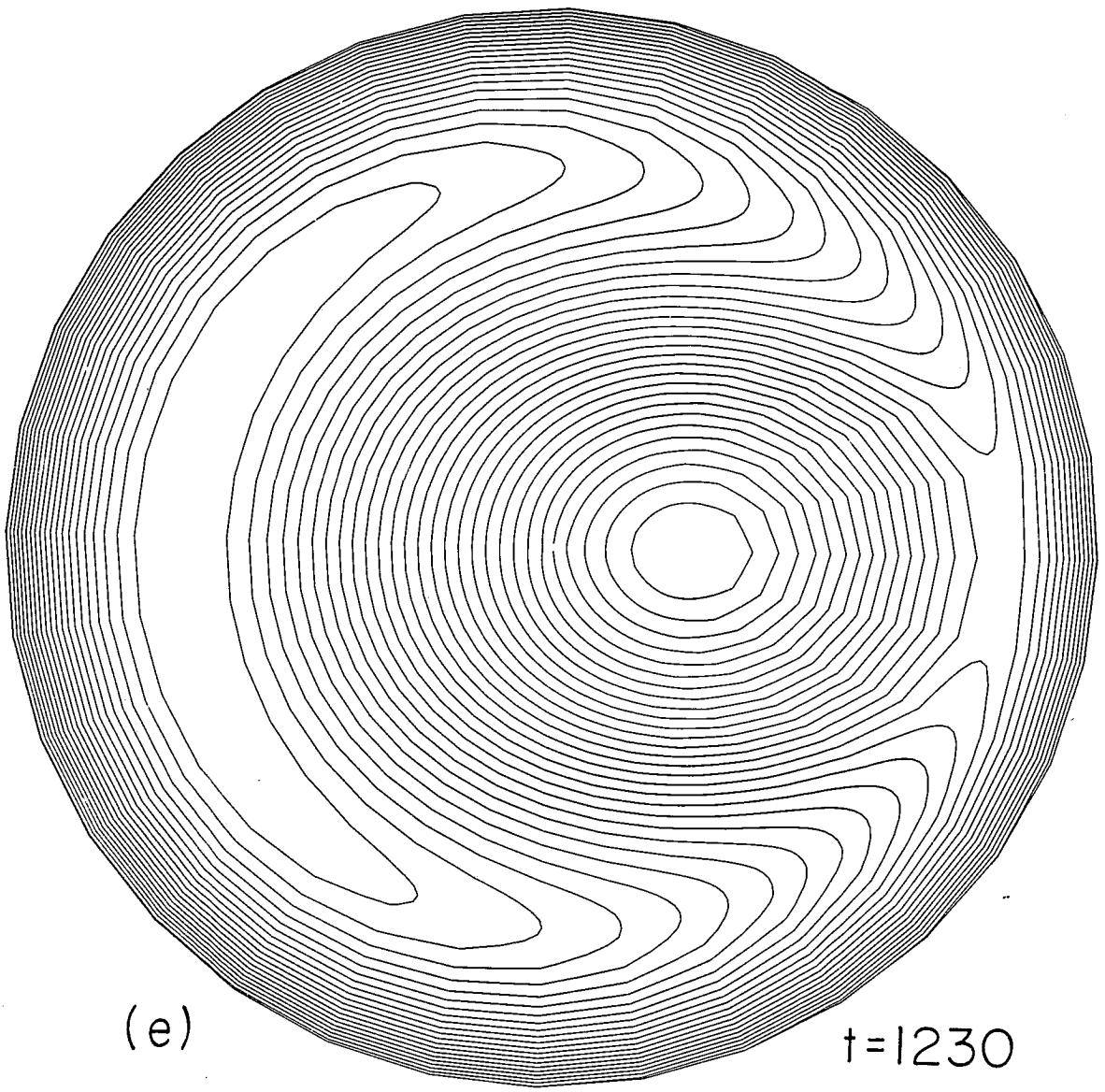

FIG. 6e

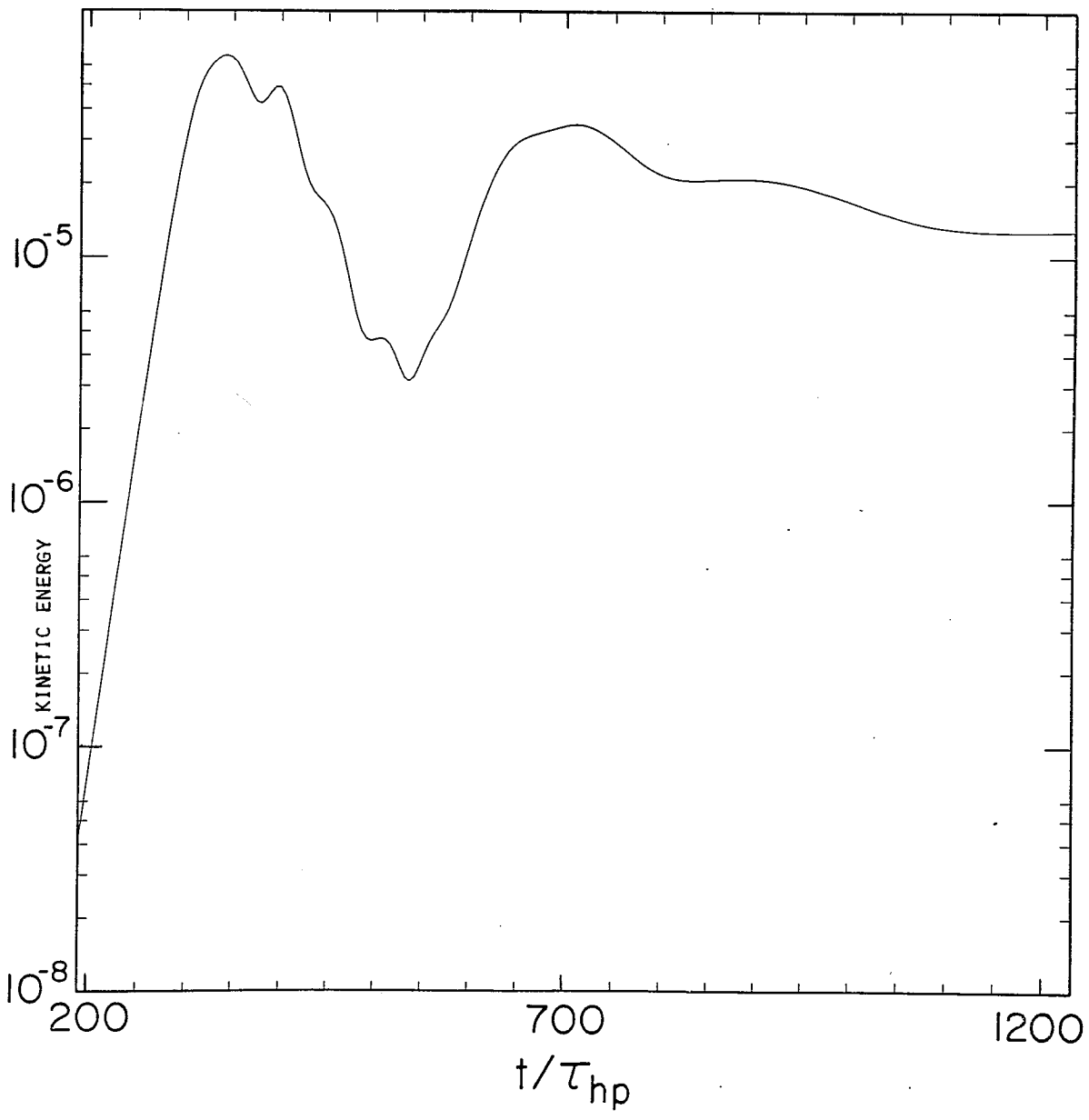

FIG. 7

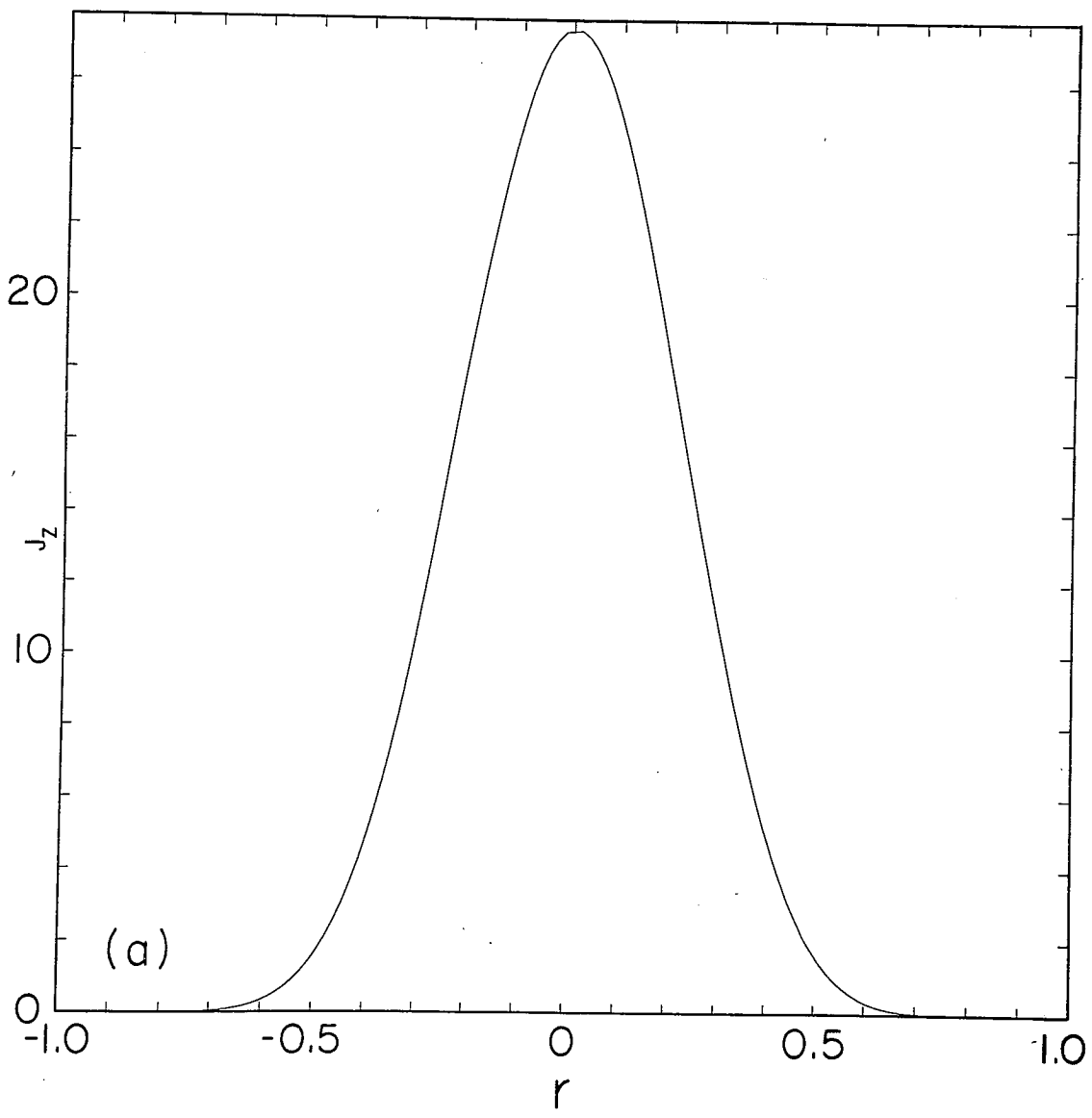

FIG. 8a

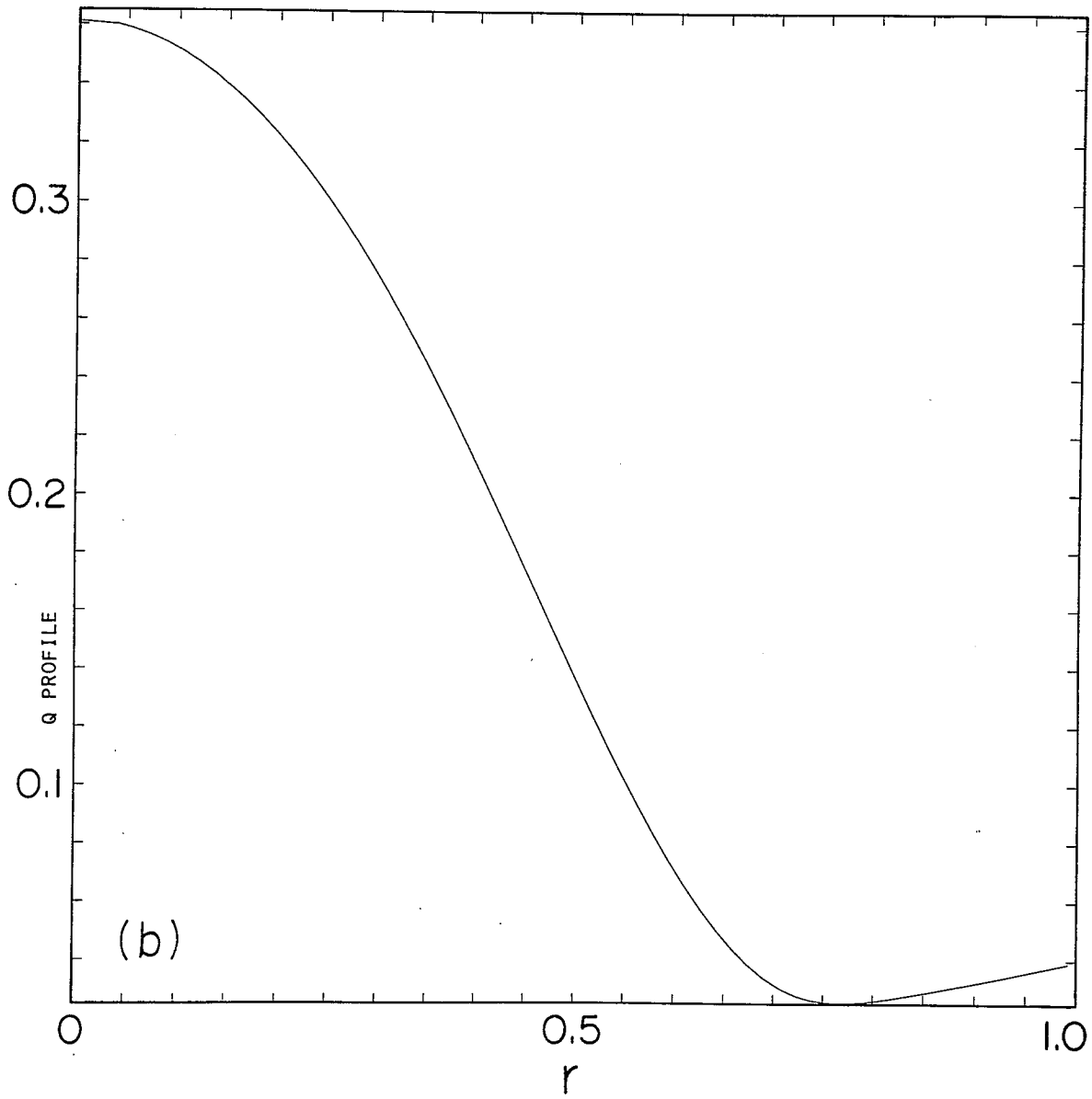

FIG. 8b

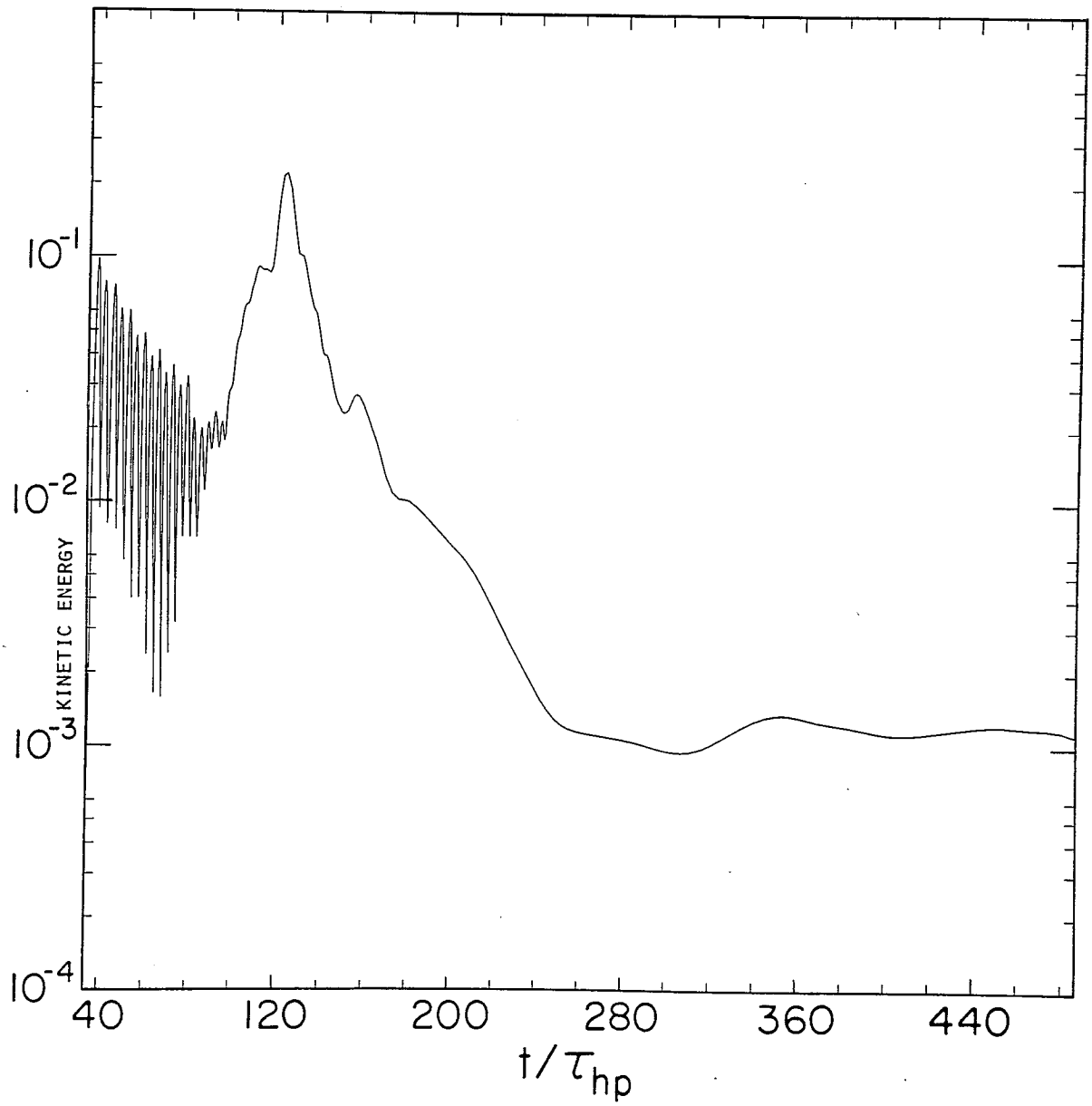

FIG. 9

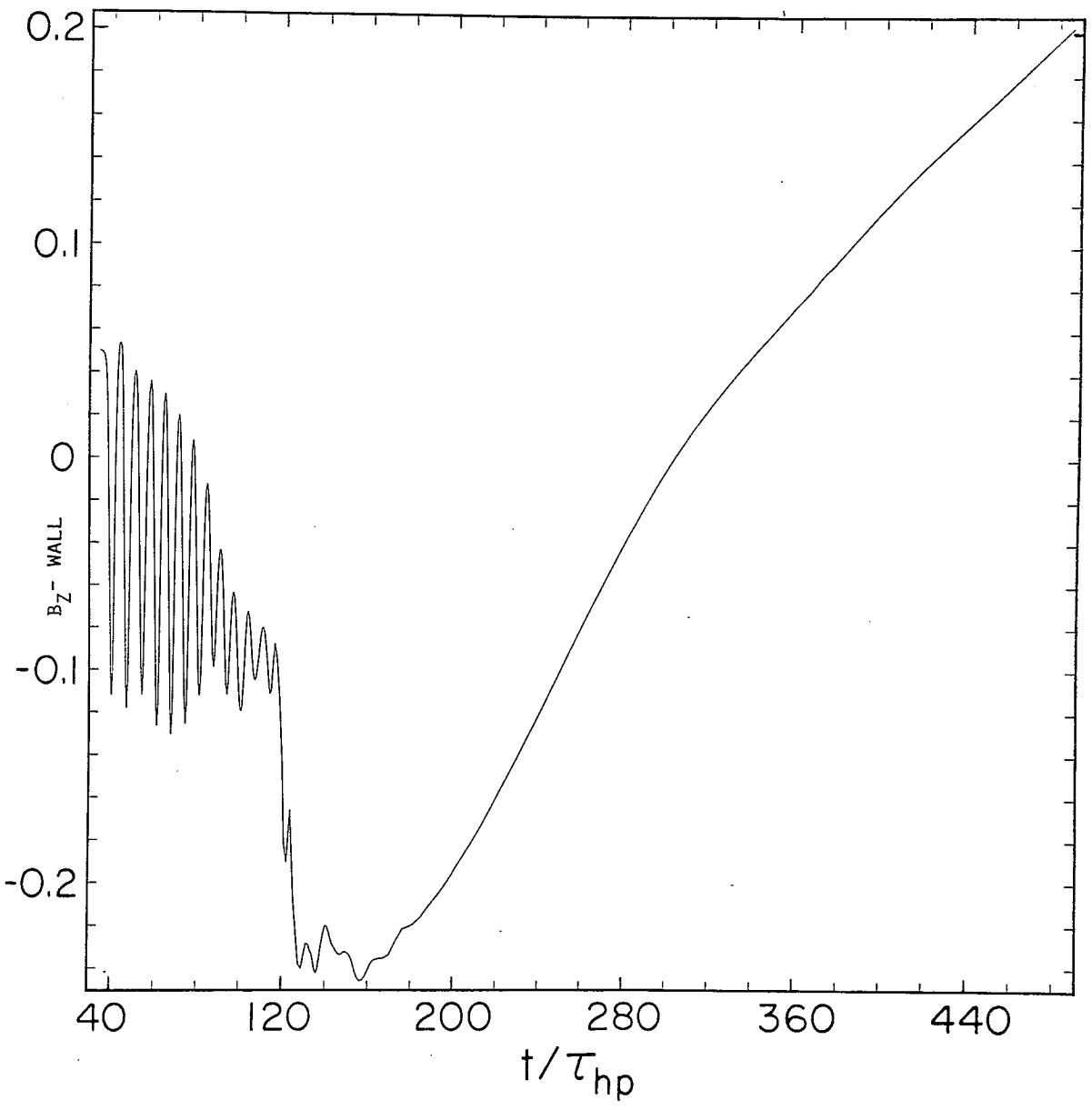

FIG. 10

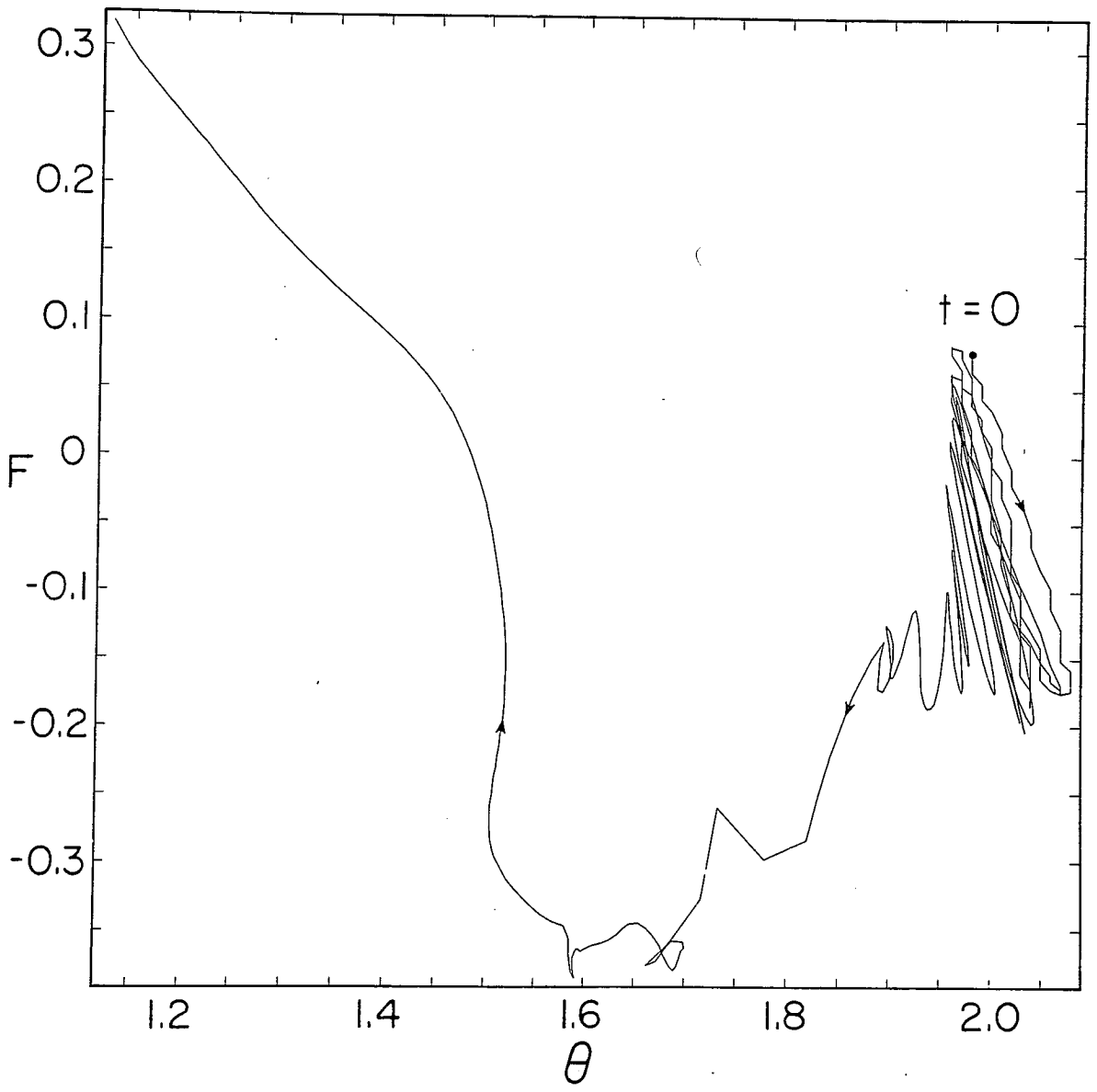

FIG. 11

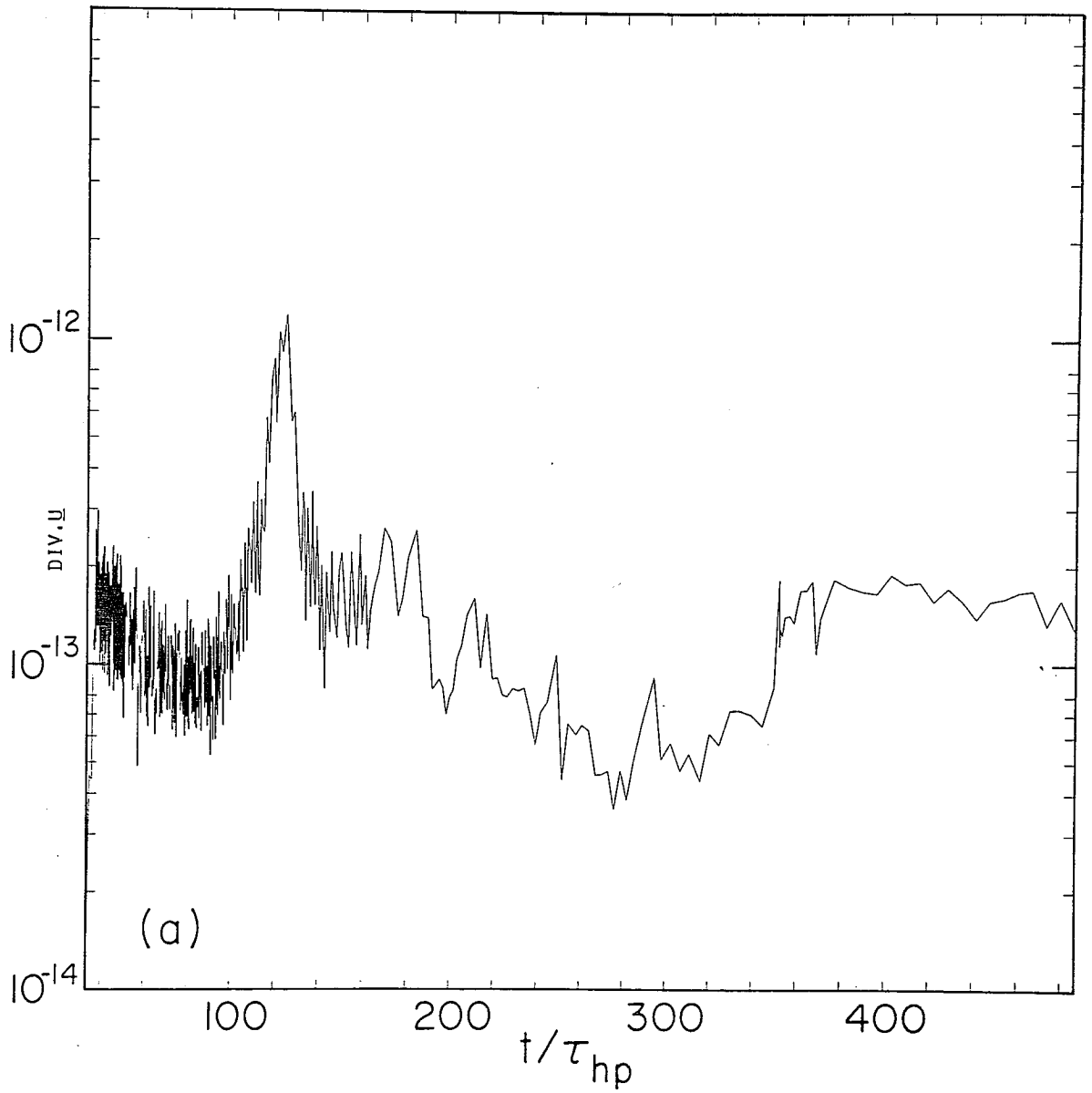

FIG. 12a

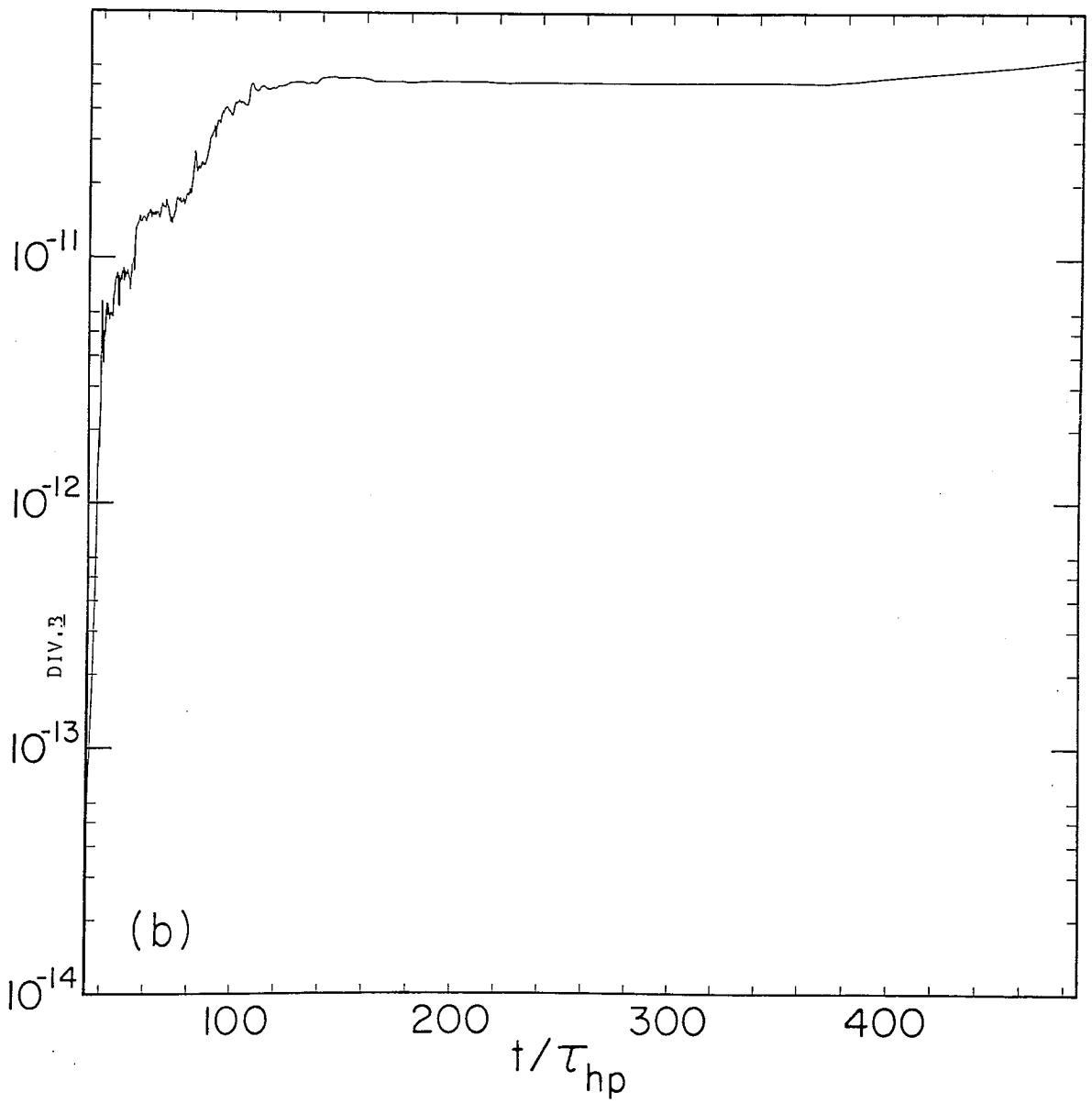

FIG. 12b